Measurement Report: Cloud condensation nuclei (CCN) activity in the South China Sea from shipborne observations during summer and winter of 2021: seasonal variation and anthropogenic influence.

Hengjia Ou[1], Mingfu Cai[2*], Yongyun Zhang[1], Xue Ni[1], Baoling Liang[3], Qibin Sun[4,5],

Shixin Mai[1], Cuizhi Sun[6], Shengzhen Zhou[1], Haichao Wang[1], Jiaren Sun[2], Jun Zhao[1*]

[1]School of Atmospheric Sciences, Guangdong Province Key Laboratory for Climate Change and Natural

Disaster Studies, Southern Marine Science and Engineering Guangdong Laboratory (Zhuhai), Sun Yat-

sen University, Zhuhai, Guangdong 519082, China

[2]Guangdong Province Engineering Laboratory for Air Pollution Control, Guangdong Provincial Key

Laboratory of Water and Air Pollution Control, South China Institute of Environmental Sciences, MEE,

Guangzhou 510655, China

[3]Guangzhou Sub-branch of Guangdong Ecological and Environmental Monitoring Center, Guangzhou

510006, China

[4]Dongguan Meteorological Bureau, Dongguan, Guangdong, 523086, China

[5]Dongguan Engineering Technology Research Center of Urban Eco-Environmental Meteorology,

Dongguan, Guangdong, 523086, China

[6]Southern Marine Science and Engineering Guangdong Laboratory (Zhuhai), Zhuhai, Guangdong

519082, China

Correspondence: Mingfu Cai (caimingfu@scies.org) and Jun Zhao (zhaojun23@mail.sysu.edu.cn)

Abstract

Understanding seasonal variations in cloud condensation nuclei (CCN) activity and the impact of anthropogenic emissions in marine environments is crucial for assessing climate change. This study presents findings from two shipborne observations conducted in the South China Sea (SCS) during the summer and winter of 2021. In summer, higher particle number concentrations but lower mass concentrations of non-refractory submicron particles (NR-PM$_1$) were observed, driven by Aitken mode particle dominance. In contrast, winter showed a more balanced distribution between Aitken and Accumulation mode particles. Summer particles were more hygroscopic, exhibiting higher activation ratios (ARs) at all supersaturation (SS) levels. Distinct air mass periods were identified: in summer, terrestrial air masses from Luzon ("Luzon" period), the Indochinese Peninsula ("Indochinese Peninsula" period), and marine air masses; in winter, periods were influenced by Mainland China ("Mainland China" period), a mix of Mainland China and marine air masses ("Mixed" period), and purely marine air masses. The "Luzon" period in summer exhibited the highest particle number concentration, especially in the Aitken mode, resulting in the highest CCN number concentration (N$_{CCN}$). Aerosol hygroscopicity was higher during the "Indochinese Peninsula" period compared to the "Luzon" period, leading to a higher bulk AR due to the combination of higher hygroscopicity and a greater fraction of accumulation mode particles. The "Mainland China" period in winter showed a high nitrate fraction in the NR-PM$_1$, but the inorganic fraction was similar to it in "Luzon" period, resulting in comparable hygroscopicity at low SS to the "Luzon" period. However, smaller particle hygroscopicity was significantly lower in the "Mainland China" period compared to summer. The "Mixed" period in winter exhibited a higher fraction of accumulation mode particles, causing a higher bulk AR compared to the "Mainland China" period. Overall, summer terrestrial air masses increased the Aitken mode particle and CCN concentration, while winter terrestrial air masses led to higher concentration of large particles and lower hygroscopicity of fine particles. CCN closure analysis, considering aerosol composition and mixing state, revealed that summer aerosols were primarily internally mixed, whereas smaller aerosols in winter were primarily externally mixed. The potential effect of undetected sea salt may lead to an underestimation of aerosol hygroscopicity in summer. This study highlights significant seasonal differences in aerosol properties and the impact of different types of terrestrial air masses on CCN activity in the SCS, contributing to our understanding of regional climate influences.

1.Introduction

Aerosols can act as cloud condensation nuclei (CCN), influencing cloud formation, lifespan, and albedo, thus indirectly impacting global radiative balance (Fletcher et al., 2011; Albrecht, 1989). The aerosol-cloud interaction currently represents the largest uncertainty in radiative forcing within climate models, ranging from -1.7 to -0.3 W m^{-2} (IPCC, 2021). This uncertainty can be partially attributed to the significant spatiotemporal variability in the aerosol size distribution and the ability of atmospheric aerosol particles acting as CCN (CCN activity) (Fitzgerald, 1973; Jimenez et al., 2009; Sihto et al., 2011). Thus, field measurements of aerosol size distribution and physicochemical properties are needed to better understand the radiative forcing exerted by atmospheric aerosol particles.

Previous studies suggest that particle number size distribution (PNSD) is a primary factor influencing CCN concentrations (Dusek et al., 2006; Rose et al., 2010; Pöhlker et al., 2016; Burkart et al., 2011). The PNSD can account for 84–96% of the variability in the CCN concentrations (N_{CCN}) (Dusek et al., 2006), while CCN activities may also play a significant role in the N_{CCN} (Quinn et al., 2008; Cai et al., 2018; Ovadnevaite et al., 2017; Liu et al., 2018; Crosbie et al., 2015), which are primarily governed by the particle size, chemical composition, mixing state, surface tension, and hygroscopicity (Köhler, 1936; Seinfeld and Pandis, 2016). Among these factors, the impact of hygroscopicity on CCN activities has received great attention in recent years (Petters and Kreidenweis, 2007; Ajith et al., 2022; Rose et al., 2010). Petters and Kreidenweis (2007) proposed the κ- Köhler theory based on the Köhler theory to quantify the ability of aerosol particles to absorb moisture and become CCN based on the aerosol hygroscopicity parameters (κ). Ajith et al. (2022) showed that 64% of particles can be activated as CCN when κ is equal to 0.37, whereas when κ decreases to 0.23, only 48% of particles can be activated in the tropical coastal area.

Significant seasonal variations in PNSD and hygroscopicity under both terrestrial and marine environments were observed in previous field observations, leading to the seasonal variations in N_{CCN} (Crosbie et al., 2015; Schmale et al., 2018; Burkart et al., 2011; Bougiatioti et al., 2009; Sihto et al., 2011; Leena et al., 2016; Ross et al., 2003; Gras and Keywood, 2017; Quinn et al., 2019). Crosbie et al. (2015) revealed that in the urban area of Arizona particles had larger sizes, higher hygroscopicity, and N_{CCN} was also higher during winter, while a higher abundance of smaller particles was observed during summer owing to stronger photochemical reactions. In pristine environments like mountain, coastal, and forested

81   regions, seasonal variations in N_{CCN} and PNSD were more pronounced than urban and rural areas

82   (Schmale et al., 2018). Pöhlker et al. (2016) observed significant differences in N_{CCN} between the wet

83   and dry seasons in the Amazon rainforest, while the κ values remained relatively stable. They also noted

84   increased particle concentrations and aerosol hygroscopicity, both subject to the impact of long-range

85   transport originating from anthropogenic emissions. Observations in marine areas during different

86   seasons are relatively scarce compared with those in inland areas. Gras (1995) found that both particle

87   concentration and N_{CCN} in the Southern Ocean reached their peaks during summer and gradually decrease

88   to their valleys in winter. Quinn et al. (2019) showed that sea spray aerosols make a relatively significant

89   contribution to N_{CCN} only during winter in the Western North Atlantic, while in other seasons, the primary

90   contribution comes from biogenic aerosols oxidized from dimethyl sulfide (DMS). Zheng et al. (2020)

91   revealed that sulfate dominates the particle condensational growth to CCN sizes during summer in the

92   Eastern North Atlantic, while secondary organic aerosols played a significant role in particle growth

93   throughout all seasons. These results indicate that CCN activity and concentration could vary in a large

94   range during different seasons. Thus, further observations across different seasons in marine

95   environments are needed to enhance our understanding of marine CCN activities and their seasonal

96   variations.

97   The South China Sea (SCS), located in Southeast Asia and bordered by China, the Indochinese

98   Peninsula, and Maritime Southeast Asia, is significantly influenced by air pollutants transported through

99   terrestrial air masses. Studies have shown that these pollutants play a crucial role in determining aerosol

100   concentration and properties in the region (Atwood et al., 2017; Xiao et al., 2017; Geng et al., 2019;

101   Liang et al., 2021; Sun et al., 2023; Qin et al., 2024). For instance, Xiao et al. (2017) reported that 69.7%

102   of nitrate and 57.5% of sulfate in the SCS originated from fossil fuel combustion, particularly coal

103   burning in Chinese coastal regions. Additionally, Liang et al. (2021) and Sun et al. (2023) observed an

104   increase in the organic fraction and concentration of submicron aerosols when the region was influenced

105   by terrestrial air masses from Mainland China and the Indochinese Peninsula in the northern SCS. Further

106   studies highlighted the variation in aerosol properties under different air mass influences. Atwood et al.

107   (2017) found a significant bimodal particle distribution with a κ value of 0.65 in the southern SCS under

108   marine air mass influence, whereas a unimodal distribution with a κ of 0.4 was observed under

109   continental air mass influence.

4

The SCS experiences a typical monsoon climate with distinct seasonal wind direction changes (Wang et al., 2009). The northeast monsoon, occurring from November to March, is characterized by stronger average wind speeds and longer period compared to the southwest monsoon, which dominates from June to August. The transitional periods occur from April to May and September to October. During the northeast monsoon, air pollutants are primarily transported to the SCS by terrestrial air masses from China (Xiao et al., 2017; Liu et al., 2014; Geng et al., 2019). In contrast, during the summer, pollutants mainly originate from terrestrial air masses from the Indochinese Peninsula and Maritime Southeast Asia (Geng et al., 2019; Liang et al., 2021; Sun et al., 2023). These varying sources of anthropogenic emissions exert different impacts on CCN activity differently across seasons. Additionally, when the marine boundary layer over the SCS is influenced by various natural and anthropogenic sources, resulting in altered aerosol properties, the characteristics of cumulus clouds are correspondingly affected (Miller et al., 2023). This indicates that aerosol-cloud interactions vary between winter and summer seasons. However, due to limited observational data, our understanding of seasonal variations in CCN activity in the SCS remains incomplete. Conducting comprehensive observational studies on CCN activity across different seasons is essential for improving our understanding of aerosol-cloud interactions on the SCS.

In this study, we conducted two shipborne observations in the SCS during summer (May 5–June 9, 2021) and winter (December 19–29, 2021). Our observations with online instruments focused on measuring aerosol chemical composition, PNSD, and CCN activation in the region. Our results provide valuable insights into the differences in CCN activity between winter and summer, as well as the influence of different types of terrestrial air masses on CCN activity in the SCS across different seasons.

2. Methodology

2.1 Cruise information and onboard measurements

2.1.1 Cruise information

This study consists of two research cruises conducted during the summer and winter of 2021, respectively. These two cruises were interdisciplinary scientific expeditions, integrating fields such as marine geology, oceanography, and atmospheric environment. The primary objective in atmospheric environment was to investigate the impact of summer and winter monsoons on the atmospheric environment of the South China Sea (SCS). The summer and winter cruises were carried out respectively by the vessels "Tan Kah Kee" and "Sun Yat-sen University". The "Tan Kah Kee" is an oceanographic

research vessel with a length of 77.7 meters, a beam of 16.24 meters, and a displacement of 3611 tons. The "Sun Yat-sen University" is a comprehensive oceanographic training vessel with a total length of 114.3 meters, a beam of 19.4 meters, and a displacement of 6880 tons.

The first cruise was from May 5th to June 9th, 2021. The cruise started from Xiamen Port and traversed from the northern to the central-southern South China Sea, and then circled back near Hainan Island, and finally returned to Xiamen Port. The second cruise was from December 19th to December 29th, 2021. It began from Gaolan Port in Zhuhai and reached the vicinity of Yongxing Island, and ultimately returned to Gaolan Port (Fig. 1a). Unfortunately, due to adverse weather conditions, such as strong winter monsoon winds causing poor sea conditions, and the fact that it was the first scientific deployment of the research vessel Sun Yat-sen University, the winter cruise had a shorter duration and covered a narrower spatial range, remaining only in the northern SCS (Fig. S1), compared to the summer cruise. On both cruises, most of the instruments were housed in a single compartment and the sampling lines were extended from the window of the compartment to the height of the ship's bridge (~17 m above sea level) (Fig. 1a).

2.1.2 Size-resolved cloud condensation nuclei activity measurement

The size-resolved CCN activity was measured using the scanning mobility CCN analysis (SMCA) method proposed by Moore et al. (2010), employing a combination of a scanning mobility particle sizer (SMPS) system and a cloud condensation nuclei counter (CCNc-200, DMT Inc., USA) (Fig. S2). The SMPS system consisted of a differential mobility analyzer (DMA; model 3082, TSI., Inc.) and a condensation particle counter (CPC; model 3756, TSI Inc.). The SMPS and the CCNc system were used to measure PNSD and size-resolved CCN number concentration at a mobility size range of 10–500 nm and 10–593 nm in summer and winter campaign, respectively. Unfortunately, due to the malfunction of flow sensor in the column B on both cruises, only the data from column A is presented in this study. During the SMCA measurement, the particles were first passed through a Nafion dryer to remove moisture, then neutralized using a neutralizer. After that, they were subjected to size selection with a DMA. The particles were then split between a CPC (1 L min^{-1}) for particle concentration measurement and a CCNc (0.5 L min^{-1}) for CCN measurement at a specific supersaturation (SS). To maintain sample flow through the DMA, dilution air (0.5 L min^{-1}) was added to the CPC inlet stream. The effect of the dilution air was accounted for in the PNSD data processing (Fig. S2). The supersaturation of the CCNc

was set at 0.2 %, 0.4 %, and 0.7 % in summer campaign and 0.1%, 0.2 %, 0.4 %, and 0.7 % in winter

campaign, respectively. During the measurement process, each supersaturation level was held constant

for 20 minutes, with the DMA completing a full scanning cycle every 5 minutes. During the

measurements, supersaturation levels varied incrementally between 0.1% and 0.2%, 0.2% and 0.4%, and

0.4% and 0.7%, with temperature stabilization times ranging from a few seconds to several tens of

seconds. However, reducing the supersaturation from 0.7% to 0.1% or 0.2% required approximately 5

minutes for stabilization. For data processing, only instances where the temperature remained stable

throughout the DMA scanning phase were included in the analysis. Before the measurements, the CCNc

was calibrated with ammonium sulfate ($(NH_4)_2SO_4$) particles at each set SS. Detailed description of the

instrument configuration and calibration can be found in Cai et al. (2018). The uncertainty in the

instrument's measurement of size-resolved particle number concentration is approximately 5%-6%

(Morre et al. 2010).

2.1.3 Aerosol chemical composition measurement

The chemical composition of atmospheric non-refractory submicron particulate matter (NR-PM$_1$),

including sulfate, nitrate, organics, ammonium, and chloride, was measured using an online time-of-

flight ACSM (ToF-ACSM; Aerodyne Inc., USA). The sampling time of the ToF-ACSM was

approximately 10 min. The ionization efficiency (IE) and relative ionization efficiency (RIE) values of

the instrument were calibrated using ammonium nitrate (NH_4NO_3) and ammonium sulfate ($(NH_4)_2SO_4$)

both before the start and after the completion of the campaigns. The calibration gives an IE value of

103.4 ions pg^{-1} and 98.9 ions pg^{-1} for nitrate in summer and winter cruises, respectively. The RIE values

for ammonium were 3.31 and 3.33 during the summer and winter, respectively, while the ones for sulfate

were 1.02 and 0.81 during the summer and winter, respectively. The collection efficiency (CE) was

determined as shown in Sun et al. (2023) and time-independent CE values were used in this study.

Detailed CE calculation and discussion can be found in the supplementary (Text S1, and Fig. S3). The

values obtained using the time-independent CE method show a deviation of approximately 3% compared

to those obtained with a constant CE of 0.5. Assuming an average aerosol density of 1.5 g cm^{-3} (Geller

et al., 2006), the mass concentrations measured by the SMPS and ToF-ACSM exhibit a strong overall

correlation, with correlation coefficients of 0.84 in summer and 0.93 in winter. During the pre-onset

phase of the summer monsoon (prior to May 24), periodic discrepancies were observed between the

197 <u>ACSM and SMPS data, likely due to the influence of refractory aerosol (ie. Black carbon). This issue is</u>

198 <u>discussed in detail in Text S1.</u> The black carbon (BC) mass concentrations were measured using an

199 aethalometer (Model AE33, Magee Scientific, USA) with a 1-minute time resolution (Drinovec et al.,

200 2015). Notably, the BC mass concentrations obtained from AE33 are referred to as equivalent BC mass

201 concentrations, as they represent the combined light absorption of BC at 880 nm. Prior to entering the

202 AE33, the sampled air was passed through a $PM_{2.5}$ cyclone (BGI Inc., Waltham, MA, USA) to exclude

203 particles larger than 2.5 µm.

204 **2.1.4 Meteorological parameter measurements**

205 The meteorological elements, including temperature, relative humility (RH), wind speed, and wind

206 direction, were measured by the combined automatic weather station (AWS430, Vaisala Inc., Finland)

207 onboard the vessels (Sun et al., 2024). During the winter cruises, meteorology data before 12.22 was

208 missed due to the calibration for the automatic weather station (WXT536, Vaisala Inc., Finland) before

209 12.22. The timeseries of meteorological data were presented in Fig. S5. The AWS430 provides

210 measurement accuracies of ±2% for wind speed, ±2% for wind direction, ±0.3°C for temperature, and

211 ±1% for relative humidity (within the range of 0–90%). Similarly, the WXT536 offers accuracies of ±3%

212 for wind speed, ±3% for wind direction, ±0.3°C for temperature, and ±3% for relative humidity (within

213 the range of 0–90%) (www.vaisala.com).

214 **2.2 Data analysis**

215 **2.2.1 CCN activation**

216 The size-resolved number concentration of total particle and cloud condensation nuclei were

217 obtained from the SMPS and CCNc thourgh the SMCA method. The activation diameter was determined

218 by fitting the activation ratio (AR, N_{CCN}/N_{CN}) and dry diameter at each supersaturation through the

219 following equation:

220 $$AR = \frac{B}{1+\left(\frac{D_P}{D_{50}}\right)^C},$$ (1)

221 where AR indicates the size-resolved AR, D_P represents dry particle diameter (nm); B, C, and D_{50} are the

222 three fitting parameters, representing the asymptote, the slope, and the inflection point of the sigmoid,

223 respectively (Moore et al., 2010). The D_{50} parameter, also known as the critical diameter, corresponds to

the particle size at which 50% of the particles are activated at a specific SS. The fitting results from

SMCA method measured in this study are presented in Fig. S6.

The hygroscopicity parameter (κ) which represents CCN activity according to κ-Köhler equation is

calculated as follows (Petters and Kreidenweis, 2007):

$$\kappa = \frac{4A^3}{27D_{50}^3(\ln S_C)^2}, \quad A = \frac{4\sigma_{s/a}M_w}{RT\rho_w} \tag{2}$$

where ρ_w is the density of pure water (about 997.04 kg m^{-3} at 298.15 K), M_W is the molecular weight of

water (0.018 kg mol^{-1}), $\sigma_{s/a}$ corresponds to the surface tension of the solution-air interface and is assumed

to be equal to the surface tension of pure water ($\sigma_{s/a}$=0.0728 N m^{-1} at 298.15 K), R is the universal gas

constant (8.314 J mol^{-1} K^{-1}), T denotes thermodynamic temperature in kelvin (298.15 K), and D_{50} is the

critical diameter (in m). Additionally, it is noting that the estimated κ values refer to particles with the

D_{50}.

According to κ-Köhler theory, in the following discussion, the hygroscopicity of small particles is

associated with hygroscopicity at high SS, whereas the hygroscopicity of large particles is linked to

hygroscopicity at low SS.

During part of the summer measurement period, the D_{50} at 0.7% supersaturation ranged between 30

and 40. However, due to lower concentrations during these times, instrument noise introduced greater

measurement uncertainty, as demonstrated in Fig. S7. Consequently, the average D_{50} and κ at 0.7% SS

are not included in Table 1.

2.2.2 Closure Method

According to Petters and Kreidenweis. (2007), κ can be predicted by a simple mixing rule based on

chemical volume fractions:

$$\kappa_{sim} = \sum_i \varepsilon_i \kappa_i \tag{3}$$

where ε_i and κ_i are the volume fraction and hygroscopicity parameter for the specific dry component

in the mixture. We obtained ε from aerosol chemical composition measured by the ToF-ACSM. In this

study, κ for $(NH_4)_2SO_4$ (0.48), NH_4NO_3 (0.58), and NaCl (1.1) represent the κ of SO_4^{2-}, NO_3^-, and Cl$^-$

provided by the ToF-ACSM (Huang et al., 2022). Besides, the κ of organic was 0.1 at this study according

to Huang et al. (2022). The density of $(NH_4)_2SO_4$, NH_4NO_3, NaCl and organic are 1769 kg m^{-3}, 1720 kg

m^{-3}, 2165 kg m^{-3}, and 1400 kg m^{-3} (Huang et al., 2022; Gysel et al., 2007).

9

2.2.3 CCN concentration and activation ratio calculation

Due to the malfunction of the column B, the CCN concentration (N_{CCN}) was calculated based on the size-resolved AR at a specific SS from SMCA method and observed particle number concentration. It can be calculated by the following equation (Cai et al., 2018):

$$N_{CCN}(SS) = \int_0^\infty AR(SS, D_P) N_{CN}(D_P) dD_p \qquad (4)$$

where $N_{CCN}(SS)$ is the CCN concentration at a specific SS, $AR(SS, D_p)$ is the ratio of N_{CCN} at a specific SS to N_{CN} on a specific diameter from the SMCA method and $N_{CN}(D_P)$ is the particle number concentration at a specific diameter (Dp). Due to the absence of direct measurements for total N_{CCN}, we refer to the N_{CCN} derived from Eq. (4) as observed values ($N_{CCN,obs}$) in this study. Previous research has shown that this method (size-resolved CCN from one column in CCNc-200) provides results closely matching those obtained from direct measurement (from another column in CCNc-200), supporting its reliability (Meng et al., 2014; Lathem and Nenes, 2011).

The N_{CCN} (referred as $N_{CCN,sim}(SS)$) can be predicted by D_{50} from closure method ($D_{50,sim}(SS)$) and N_{CN} according to following equation (Jurányi et al., 2011):

$$N_{CCN,sim}(SS) = \int_{D_{50,sim}(SS)}^\infty N_{CN}(D_P) dD_p \qquad (5)$$

where the $D_{50,sim}(SS)$ is calculated based on the eq. (2) and (3).

The bulk AR at a specific SS can be calculated by:

$$AR(SS) = \frac{N_{CCN,obs}(SS)}{N_{CN,tot}} \qquad (6)$$

where the $N_{CN,tot}$ represents the total particle number concentration.

To investigate the impact of the fraction and mixing state of aerosol on N_{CCN}, two CCN simulation schemes are applied in this study (Patel et al., 2021).

(1) Internal-mixed scheme: the aerosol composition from the ToF-ACSM was assumed to be size-independent and internally mixed. All aerosols have an identical chemical composition in the whole size range. N_{CCN} is calculated by κ_{sim} and measured PNSD according to Eq. (2), Eq. (3), and Eq. (5) (Fig. S8a).

(2) External-mixed scheme: the aerosol composition from the ToF-ACSM was assumed to be size-independent and externally mixed. Four types of aerosols (($NH_4)_2SO_4$, NH_4NO_3, $NaCl$ and organic) are assumed to have the same proportion for all sizes. The D_{50} from each species was

280   calculated by Eq. (2) according to their κ values mentioned in 2.2.2. N_{CCN} is calculated

281   according to the Eq. (5) (Fig. S8b and Table S1).

282   To access the simulation result from these two schemes, normalized mean bias (NMB) was used in

283 this study:

284      $NMB = \frac{\sum(N_{CCN,sim} - N_{CCN,obs})}{\sum N_{CCN,obs}}$ (7)

285 where $N_{CCN,sim}$ is the simulated N_{CCN} from two schemes, and $N_{CCN,obs}$ is the observed N_{CCN}.

286 **2.2.4 Fitting of log-normal modes to particle number size distributions**

287   The multi-lognormal distribution function (Eq. (8)) is used to parameterize and optimize the

288 descriptions of the measured PNSD (Heintzenberg, 1994) and is widely applied in aerosol research (Cai

289 et al, 2020; Boyer et al., 2023; Zhu and Wang, 2024). An automatic mode-fitting algorithm (Hussein et

290 al., 2005) is used to generate the model-fitted results.

291      $f\left(D_p, \bar{D}_{pg,i}, N_i, \sigma_{g,i}\right) = \sum_{i=1}^{n} \frac{N_i}{\sqrt{2\pi}\log(\sigma_{g,i})} \times \exp\left[-\frac{\left[\log D_p - \log \bar{D}_{pg,i}\right]^2}{2(\log \sigma_{g,i})^2}\right]$ (8)

292   where D_P is the diameter of a particle. Each lognormal mode is characterized by three parameters:

293 the mode number concentration (N_i), geometric variance ($\sigma_{g,i}$), and geometric mean diameter (GMD,

294 $\bar{D}_{pg,i}$). The total number of lognormal modes used to describe the PNSD is denoted by n. These modes

295 are fitted using an algorithm applied to each particle size distribution, with one to three log-normal

296 distributions used per time step. The algorithm classifies the PNSD into nucleation, Aitken, and

297 accumulation modes based on their geometric mean diameters (GMDs). The GMD for nucleation modes

298 (GMD1) typically ranges from 3 to 30 nm, for Aitken modes (GMD2) from 30 to 100 nm, and for

299 accumulation modes (GMD3) above 100 nm (Heintzenberg, 1994; Hussein et al., 2005; Zhu and Wang,

300 2024).

301 **2.2.5 Backward trajectory simulation and cluster analysis**

302   Backward trajectory calculations were performed using the MeteoInfo, an open-source software

303 (Wang, 2014) to determine potential source origins. Weekly GDAS1 (Global Data Assimilation System

304 at a resolution of 1°) files were downloaded from the NOAA Air Resource Laboratory (ARL) website

305 (https://www.ready.noaa.gov/gdas1.php). The calculation of backward trajectories is performed every

306 1hour based on the location mentioned below, generating 72-hour backward trajectories at 500m.

307   To clarify the sources of air masses, the cluster analysis was applied in this study, which was

308   performed by TrajStat, a plug-in module of MeteoInfo, based on k-means method

309   (http://meteothink.org/docs/trajstat/cluster_cal.html). According to the report by the China

310   Meteorological Administration (Chao et al., 2022), the summer monsoon in 2021 broke out during the

311   sixth pentad of May. Therefore, based on the timing of the monsoon onset and the actual trajectory of the

312   ship, we selected two representative midpoints of the ship track for backward trajectory calculations and

313   cluster analysis in summer: the midpoint of the ship's track before the onset of the summer monsoon

314   (May 5-23) and the midpoint of the track after the summer monsoon began (May 24-June 9). In the

315   winter cruise, backward trajectories calculation and cluster analysis were performed at two specific

316   locations: the ship's anchorage near Big Ten-thousand Mountain Island (December 19-22 and December

317   27-29) and the midpoint between Dawan Mountain Island and Yongxing Island (December 23-26). To

318   ensure the accuracy of the backward trajectory calculations and cluster analysis, we compared the

319   trajectories at the midpoints with those from the ship's actual locations to verify consistency in air mass

320   sources (Fig. S9). Minor discrepancies may exist between the air mass origins at certain midpoints and

321   the actual ship locations. However, overall, the air mass origins at the midpoints are representative of

322   those at the actual locations. We further examined the trajectories for each cluster to verify their alignment

323   with the air mass origins they represent (Fig. S10). The results demonstrate that cluster analysis was well

324   conducted. Additionally, figure S10 illustrates the average altitude variation as the age in hours increases

325   across different periods. During summer, the altitude of the clusters remained below 880 hPa, indicating

326   that they resided within the boundary layer (about 800 hPa). While in winter, the altitude of the clusters

327   was higher than in summer, especially for the cluster during the mixed period (peaked at about 755 hPa).

328   However, these clusters were generally within or close to the boundary layer. These results suggest that

329   the back trajectories could represent the characteristics of the air masses originating from these specified

330   regions.

331   **2.2.5 Data quality control**

332   To ensure reliable atmospheric samples in the SCS and mitigate the influence of research vessel

333   emissions, we applied the following data processing procedures (Huang et al., 2018; Cai et al., 2020;

334   Liang et al., 2021).

335   Firstly, we identified organic compounds, black carbon (BC), and small particulate matter (41.4 nm

336   particles) as indicators of ship emissions, recognizing their sudden peak values as indicative of the ship's

337   own emissions.

338   Secondly, we accounted for the relative positions of the ship's chimney and the sampling tube.

339   During the summer cruise, we excluded data corresponding to a relative wind direction (with respect to

340   the ship's bow) between 150° and 270° and a relative wind speed (with respect to the ship's speed) of less

341   than 2.5 m s^{-1} (Fig. S12a, Fig. S13a1, and Fig. S14a-c). During the winter cruise, we excluded data for a

342   relative wind direction between 150° and 220° and a relative wind speed of less than 2.5 m s^{-1} (Fig. S12b,

343   Fig. S13b1, and Figs. S14d-f).

344   Applying these criteria, 74.8% of the data in summer and 92.2% in winter (both at 10-minute

345   resolution) were classified as "clean" and retained for analysis. The timeseries of data before and after

346   quality control is shown in Fig. S15.

347   **3. Results and discussion**

348   **3.1 CCN concentration and aerosol characteristics over SCS in summer and winter**

349   Figure 2 presented the timeseries of PNSD (a1 and a2), NR-PM$_1$ mass concentrations and fractions

350   (b1 and b2, c1 and c2), number concentrations of CCN (d1 and d2), and hygroscopicity κ-values (e1 and

351   e2) during two campaigns in summer and winter. During the summer cruise, we observed two distinct

352   periods around the onset of the summer monsoon. The South China Sea (SCS) summer monsoon began

353   in the sixth pentad of May (Chao et al., 2022). In winter, the influence of the winter monsoon persisted

354   throughout the entire observation period (Fig. 1c). Despite our measurements being limited to the

355   northern SCS in winter, the impact of the Northeast Monsoon on the SCS was evident.

356   The average particle number concentration in summer (6966 cm^{-3}) was higher than in winter (4988

357   cm^{-3}), primarily due to the higher number concentration of Aitken-mode particles in summer (Fig. 3a-b).

358   In summer, particles were concentrated in smaller sizes, whereas in winter, particle size distribution was

359   relatively balanced between the Aitken mode (2185 cm^{-3}) and the accumulation mode (2176 cm^{-3}) (Fig.

360   3a-b).

361   The average mass concentration of NR-PM$_1$ was 3.76 μg m^{-3} in summer and increased to 9.39 μg

362   m^{-3} in winter (Fig. 3c-d). In summer, the dominant aerosol component was sulfate (45.5%), followed by

363   organics (35.8%), ammonium (12.9%), nitrate (4.0%), and chloride (1.9%) (Fig. 3c), similar to the

pattern observed in the northern SCS during the summer of 2018 (Fig. 3e) (Liang et al., 2021). However, in winter, organics became the predominant aerosol component (37%), with nitrate (22.2%) replacing sulfate (18.9%) as the highest proportion of inorganic components (Fig. 3d). Although N_{CN} was higher in summer than in winter, the particle volume size distribution indicates that a higher fraction of particles was concentrated in larger size in winter, which significantly influenced mass concentration, resulting in a higher NR-PM$_1$ concentration (Fig. S16).

The average number concentration of cloud condensation nuclei (N_{CCN}) in summer was higher than in winter at all supersaturation (SS) levels (Table 1). The ratio of N_{CCN} between summer and winter was smaller at high SS ($N_{CCN, winter}/N_{CCN,summer}$ = 0.51 and 0.54 at 0.4% SS and 0.7% SS, respectively) compared to low SS ($N_{CCN, winter}/N_{CCN,summer}$ = 0.62 at 0.2% SS), likely due to the significant difference in number concentration of Aitken-mode particles between the two seasons (Fig. 3a-b). Compared to the observation in the Yellow Sea, a region similarly influenced by terrestrial air masses from mainland China, the N_{CCN} were lower in winter, while in summer, the N_{CCN} were more comparable to those observed in the Yellow Sea (4821 cm^{-3} at 0.63% SS) (Park et al., 2018).

The aerosol hygroscopicity (κ) was higher in summer than that in winter (Table 1). Besides, the hygroscopicity pattern varied between seasons: in summer, κ increased with SS (from 0.47 to 0.54 between 0.2% SS and 0.4% SS), while in winter, κ decreased with SS (from 0.50 to 0.15 between 0.1% SS and 0.7% SS) (Fig. 3a-b). This contrasting trend may be related to the reduced sulfate fraction in smaller sizes during winter, as sulfate production via DMS oxidation is diminished due to lower sea surface temperatures in winter (18.0°C) compared to summer (29.3°C), which in turn inhibits DMS production by phytoplankton (Bates et al., 1987; Kouvarakis and Mihalopoulos, 2002). Additionally, it could be linked to the mixing state of the particles, with further discussion provided in the following sections. The winter κ pattern was similar to observations in the Western North Pacific (Table 1) (Kawana et al., 2020). Additionally, the winter κ values were comparable to those in Guangzhou (Cai et al., 2020), adjacent to the SCS, indicating that the northern SCS is influenced by air masses from Mainland China under the significant influence of the Northeast Monsoon during winter.

3.2 Anthropogenic influence on CCN concentration in different seasons

Cluster analysis revealed distinct periods influenced by various air masses. In summer, three terrestrial air mass sources were identified: Luzon Island (referred to as "Luzon"), Palawan Island, and

14

the Indochinese Peninsula, along with a marine air mass source (Fig. 4a). Given the limited influence of air masses from Palawan Island, this period was excluded from the study. Consequently, the study focused on periods dominated by air masses from Luzon ("Luzon" period), the Indochinese Peninsula ("Indochinese Peninsula" period), and marine sources ("Marine-s" period). In winter, the air mass sources included Mainland China, a mixture of Mainland China and the South China Sea (referred to as "Mixed"), and a marine source (Fig. 4b). These were classified as the "Mainland China" period, "Mixed" period, and "Marine-w" period, respectively.

As shown in figure 5, terrestrial air masses could significantly affect the aerosol chemical composition in the SCS, resulting in higher NR-PM$_1$ mass concentration and a higher fraction of organic compounds compared to those influenced by marine air masses. Additionally, the particles number concentration in the accumulation mode and the N$_{CCN}$ at low supersaturation (SS) were higher during periods influenced by terrestrial air masses ("Luzon" period) than those during marine air mass periods (Table 2). Notably, we were able to obtain an accurate D$_{50}$ at 0.7% supersaturation only during the "Luzon" period in summer. Due to the relatively lower hygroscopicity compared to other summer periods, the corresponding D$_{50}$ at 0.7% SS ranged between 40 and 60 nm, with relatively high concentration of CN and CCN (Fig. S7), allowing for a more precise measurement of D$_{50}$. As a result, the κ at 0.7% SS shown in Fig. 7 was specific to the Luzon period in summer.

In summer, the "Luzon" period exhibited the highest N$_{CN}$, attributed to the elevated particle concentration in the Aitken mode, compared to all other periods in both summer and winter (Fig. 6a and Table 1). This high fraction of Aitken mode particles leaded to the lowest bulk AR among the summer periods (Fig. 7a), as a larger fraction of particles centered on a size range lower than the D$_{50}$ (Fig. 7b). Furthermore, the prevalence of a higher fraction of Aitken mode particles during terrestrial air mass periods is commonly correlated with the influence of fresh anthropogenic emissions (Beddows et al., 2015), which could lower the hygroscopicity and consequently suppress the bulk AR.

In the "Indochinese Peninsula" period, the N$_{CN}$ was lower than it in the "Marine-s" period (Table 2). This difference was mainly due to the variation of Aitken mode particles, while accumulation mode particles were higher during the "Indochinese Peninsula" period than in "Marine-s" period (Table 2). The "Marine-s" period primarily occurred during the transition phase before the onset of summer monsoon, when wind direction shifted from east (Luzon Island direction) to southwest (Indochinese Peninsula direction). Anthropogenic emissions from Luzon Island still affected the marine atmosphere, leading to

higher concentrations of Aitken mode particles compared to the "Indochinese Peninsula" period (Table 2). The higher fraction of accumulation mode particles and higher hygroscopicity during the "Indochinese Peninsula" period resulted in a higher bulk AR compared to the "Luzon" period. Despite a higher organic fraction in NR-PM$_1$ during the "Indochinese Peninsula" period (Fig. 5), hygroscopicity was still higher due to a higher oxidation degree of organics, indicated by a higher m/z 44 to 43 ratio (5.87 compared to 5.60 in the "Luzon" period) (Lambe et al., 2011; Jimenez et al., 2009). Additionally, higher wind speeds during this period (7.26 m s^{-1} compared to 3.18 m s^{-1} in the "Luzon" period) potentially led a higher fraction of sea salt (Huang et al., 2022), resulting a higher aerosol hygroscopicity. Unfortunately, owing to instrument limit, sea salt cannot be detected by the ToF-ACSM.

In winter, nitrate accounted for the highest fraction of NR-PM$_1$ (25.4%) during the "Mainland China" period compared to other periods (Fig. 5d). Due to similar hygroscopicity between nitrate and sulfate, as well as comparable inorganic fractions between the "Mainland China" and "Luzon" periods, κ at 0.2% SS was also similar between these two periods (0.30 and 0.33, respectively) (Fig. 7b). However, aerosol hygroscopicity at small sizes (high SS) was much lower in the "Mainland China" period than in the "Luzon" period (Fig. 7b), contributing to the low bulk AR in the "Mainland China" period (Fig. 7a). The BC mass concentration was higher during the "Mainland China" period (2.25 µg m^{-3}) compared to the "Luzon" period (0.72 µg m^{-3}). This suggests that the lower hygroscopicity in smaller particles during the "Mainland China" period may be attributed to a larger fraction of hydrophobic BC. Additionally, as discussed in Section 3.1, the reduced biological activity during winter, which results in a decline in the fraction of small-particle sulfate and an increase in the fraction of organics, may also contribute to this low hygroscopicity in small particles (at high SS, fig 7b). The similar fractions of Aitken mode and accumulation particles indicated that PNSD could not fully explain the low bulk AR in the "Mainland China" period. Overall, lower N$_{CN}$ and bulk AR in the "Mainland China" period compared to the "Luzon" period resulted in a lower N$_{CCN}$.

During the "Mixed" period, N$_{CCN}$ was lower than in the "Mainland China" period, which can be attributed to the decreased N$_{CN}$ (Table 2). However, accumulation mode particles dominated, unlike in other terrestrial air mass periods (Fig. 6), resulting in a significantly higher bulk AR compared to the "Mainland China" period. Organic aerosol hygroscopicity was also higher during the "Mixed" period, supported by a higher m/z 44 to 43 ratio (3.88 vs. 3.10 in the "Mainland China" period), which explains the greater hygroscopicity despite a higher organic fraction in NR-PM$_1$. Additionally, the lower BC

16

453 concentration in the "Mixed" period (1.20 µg m⁻³ vs. 2.25 µg m⁻³ in the "Mainland China" period)

454 suggests a smaller BC fraction. Moreover, the higher wind speeds during the "Mixed" period (10.77 m

455 s⁻¹ vs. 7.14 m s⁻¹ in the "Mainland China" period) could have increased the sea salt fraction, further

456 enhancing aerosol hygroscopicity.

457 **3.3 CCN closure analysis**

458 The CCN closure method is a widely used approach that connects CCN activity with aerosol

459 chemical composition (Cai et al., 2018; Meng et al., 2014; Deng et al., 2013). Studies have demonstrated

460 that the aerosol mixing state is crucial for accurately parameterizing CCN activity (Su et al., 2010; Wang

461 et al., 2010; Ervens et al., 2010). Moreover, the CCN closure method provides a framework for

462 investigating the influence of aerosol mixing states on CCN activity (Padró et al., 2012; Wang et al.,

463 2018; Patel et al., 2021). In this study, we applied two schemes based on the CCN closure method, as

464 described in Section 2.2.3, which consider aerosol composition and mixing state. The fitting parameters

465 and coefficient of determination (R^2) are presented in Table 3, while the fitting plots for both schemes

466 are shown in Figures S17 and S18. Besides, the NMB from these schemes was presented in Fig. 8.

467 In summer, the NMB was always lower than 0, which indicated that simulated aerosol

468 hygroscopicity was lower than observed value (Fig. 8). Sea salt which cannot be detected by the ToF-

469 ACSM may account for higher fraction in summer due to low aerosol concentration in summer (Fig. 3c),

470 resulting in the underestimation of aerosol hygroscopicity. The NMB exhibits similar trends with changes

471 in SS in all three periods in summer. Better fitting result appeared at high SS, which indicated a greater

472 underestimation of the hygroscopicity of larger particles. Besides, "Internal-mixed" scheme had more

473 precious result than it in "External-mixed" scheme in summer (Fig. 8), suggesting the aerosol was

474 primary internally mixed in summer.

475 In winter, the "External-mixed" scheme always showed a better result than "Internal-mixed" scheme

476 at high SS (0.4% SS and 0.7% SS), indicating that particles in small size were mainly externally mixed.

477 Considering the low hygroscopicity of small-sized particles in winter, it is likely that a significant fraction

478 of these particles consists of externally mixed BC, which probably originated from fresh anthropogenic

479 emissions and remains unmixed with other inorganic salts and organics. As BC ages, inorganic and

480 organic components adhere to it, which would lead to the increase of diameter and particles tended to be

481 internally mixed (Sarangi et al., 2019). This transition resulted in higher hygroscopicity in large-sized

482   particles compared to the smaller-sized particles. Besides, overestimation of aerosol hygroscopicity at

483   high SS could be owing to a higher fraction of non- or less- hygroscopic component (such as organic and

484   BC) at small particle sizes. The predicted N_{CCN} at 0.1% SS are 20%-40% lower than the observed

485   concentrations, whereas the predictions at 0.2% SS more closely match the observed values (Fig. 8). This

486   discrepancy may be due to the higher fraction of sea salt in larger particles. However, due to instrumental

487   limitations, the ToF-ACSM cannot detect BC and sea salt. Future observations including BC and sea salt

488   are needed to better assess their effects on aerosol hygroscopicity in the South China Sea (SCS). In

489   addition, further study of size-resolved aerosol composition can also enhance the understanding on CCN

490   activity in the SCS.

491   **4. Conclusion**

492   In this study, we investigated the seasonal variations of cloud condensation nuclei (CCN) activity

493   in the South China Sea (SCS) and explored the impact of anthropogenic emissions. Shipborne

494   observations were conducted during the summer (May 5–June 9) and winter (December 19–29) of 2021.

495   We measured CCN activity, chemical composition, and particle number size distribution (PNSD) using

496   several onboard instruments, including a ToF-ACSM, a CCNc, an SMPS, and an AE33. Observations

497   included periods before and after the summer monsoon onset and periods influenced by the winter

498   monsoon.

499   Our results show that particle number concentration (N_{CN}) and CCN number concentration (N_{CCN})

500   were higher in summer than in winter, while the mass concentration of non-refractory submicron

501   particulate matter (NR-PM$_1$) was lower in summer. This difference is primarily attributed to the

502   predominance of Aitken mode particles in summer, contrasted with a higher concentration of

503   accumulation mode particles in winter. Additionally, aerosol hygroscopicity and bulk AR were found to

504   be higher in summer than in winter.

505   Backward trajectory and cluster analyses identified distinct influences from various air masses. In

506   summer, we identified periods affected by terrestrial air masses from Luzon Island (the "Luzon" period)

507   and the Indochinese Peninsula (the "Indochinese Peninsula" period), alongside a period influenced by

508   marine air masses (the "Marine-s" period). In winter, the periods were influenced by terrestrial air masses

509   from Mainland China (the "Mainland China" period), a mix of Mainland China and marine sources (the

"Mixed" period), and marine air masses (the "Marine-w" period). Terrestrial air mass periods exhibited higher NR-PM$_1$ mass concentrations, organic fractions, and N$_{CCN}$, particularly at low supersaturation, compared to those influenced by marine air masses.

During the "Luzon" period, high N$_{CCN}$ was observed, attributed to high N$_{CN}$, especially in the Aitken mode. This high concentration in the Aitken mode resulted in a low bulk AR at 0.2% SS, indicating a higher fraction of primary organic aerosol with low hygroscopicity. This caused lower overall hygroscopicity compared to other summer periods. The lower ratio of m/z 44 to 43 also suggested a lower oxidation degree of organics in this period. In the "Indochinese Peninsula" period, a higher fraction of the accumulation mode particles compared to the "Luzon" period led to a higher bulk AR, combined with increased hygroscopicity.

In winter, the "Mainland China" period was characterized by a high nitrate fraction in the NR-PM$_1$. The similar inorganic fractions in the NR-PM$_1$ between the "Mainland China" and "Luzon" periods resulted in comparable aerosol hygroscopicity at low supersaturation (0.2% SS). However, at higher supersaturation levels (0.4% and 0.7% SS), the "Mainland China" period demonstrated significantly lower hygroscopicity, which led to a reduced bulk AR at elevated supersaturation. During the "Mixed" period, accumulation mode particles predominated, leading to a high bulk AR. This indicated an aging process during transport, with more oxidized organics and higher aerosol hygroscopicity. The lower black carbon (BC) fraction and the higher sea salt fraction from high wind speed contributed to higher hygroscopicity in the "Mixed" period compared to the "Mainland China" period, despite the high organic fraction.

The CCN closure analysis, considering aerosol composition and mixing state, revealed that aerosols in summer were primarily internally mixed, while in winter, small-sized aerosols were primarily externally mixed. This distinction is crucial for climate models predicting N$_{CCN}$ in the SCS. The underestimation of aerosol hygroscopicity in summer suggests that the effect of sea salt should be considered.

Our study highlights significant seasonal differences in CCN activity in the SCS and the influence of different types of terrestrial air masses. Future measurements including size-resolved aerosol composition and obtain more precise measurements of BC and sea salt are needed to better understanding CCN activity in this region. Additionally, our observation in winter focused on the CCN activity over the northern SCS, while the influence of air masses from Mainland China in remote SCS was still unclear.

Further observations in remote SCS areas could help clarify the anthropogenic influence during winter under the effect of the winter monsoon.

Supplement. The supplement related to this article is available online.

Author contributions. **HO, MC, and JZ** designed the research. **YZ**, **XN, BL, and CS** performed the measurements. **HO, MC, QS, and SM** analyzed the data. **SZ and HW** provided useful comments on the paper. **HO, MC,** and **JZ** wrote the paper with contributions from all co-authors.

Competing interests. The authors declare that they have no conflict of interest.

565   **Reference**

566   Ajith T. C, Kompalli, S. K., and Babu, S. S.: Role of Aerosol Physicochemical Properties on Aerosol

567   Hygroscopicity and Cloud Condensation Nuclei Activity in a Tropical Coastal Atmosphere, ACS Earth

568   Space Chem, 6, 1527-1542, doi:https://doi.org/10.1021/acsearthspacechem.2c00044, 2022.

569   Albrecht, B. A.: Aerosols, cloud microphysics, and fractional cloudiness, Science, 245, 1227-1230,

570   doi:https://doi.org/10.1126/science.245.4923.1227, 1989.

571   Atwood, S. A., Reid, J. S., Kreidenweis, S. M., Blake, D. R., Jonsson, H. H., Lagrosas, N. D., Xian,

572   P., Reid, E. A., Sessions, W. R., and Simpas, J. B.: Size-resolved aerosol and cloud condensation nuclei

573   (CCN) properties in the remote marine South China Sea - Part 1: Observations and source classification,

574   Atmos. Chem. Phys., 17, 1105-1123, doi:https://doi.org/10.5194/acp-17-1105-2017, 2017.

575   Bates, T. S., Cline, J. D., Gammon, R. H., and Kelly-Hansen, S. R.: Regional and seasonal variations

576   in the flux of oceanic dimethylsulfide to the atmosphere, J. Geophys. Res. Oceans, 92, 2930-2938,

577   doi:https://doi.org/10.1029/JC092iC03p02930, 1987.

578   Beddows, D. C. S., Harrison, R. M., Green, D. C., and Fuller, G. W.: Receptor modelling of both

579   particle composition and size distribution from a background site in London, UK, Atmos. Chem. Phys.,

580   15, 10107-10125, doi:https://doi.org/10.5194/acp-15-10107-2015, 2015.

581   Bougiatioti, A., Fountoukis, C., Kalivitis, N., Pandis, S. N., Nenes, A., and Mihalopoulos, N.: Cloud

582   condensation nuclei measurements in the marine boundary layer of the eastern Mediterranean: CCN

583   closure and droplet growth kinetics, Atmos. Chem. Phys., 9, 7053-7066, doi:https://doi.org/10.5194/acp-

584   9-7053-2009, 2009.

585   Boyer, M., Aliaga, D., Pernov, J. B., Angot, H., Quéléver, L. L. J., Dada, L., Heutte, B., Dall'Osto,

586   M., Beddows, D. C. S., Brasseur, Z., Beck, I., Bucci, S., Duetsch, M., Stohl, A., Laurila, T., Asmi, E.,

587   Massling, A., Thomas, D. C., Nøjgaard, J. K., Chan, T., Sharma, S., Tunved, P., Krejci, R., Hansson, H.

588   C., Bianchi, F., Lehtipalo, K., Wiedensohler, A., Weinhold, K., Kulmala, M., Petäjä, T., Sipilä, M.,

589   Schmale, J., and Jokinen, T.: A full year of aerosol size distribution data from the central Arctic under an

590   extreme positive Arctic Oscillation: insights from the Multidisciplinary drifting Observatory for the

591   Study of Arctic Climate (MOSAiC) expedition, Atmos. Chem. Phys., 23, 389-415,

592   doi:https://doi.org/10.5194/acp-23-389-2023, 2023.

593   Burkart, J., Steiner, G., Reischl, G., and Hitzenberger, R.: Long-term study of cloud condensation

594   nuclei (CCN) activation of the atmospheric aerosol in Vienna, Atmos Environ, 45, 5751-5759,

595   doi:https://doi.org/10.1016/j.atmosenv.2011.07.022, 2011.

596   Cai, M., Tan, H., Chan, C. K., Mochida, M., Hatakeyama, S., Kondo, Y., Schurman, M. I., Xu, H.,

597   Li, F., Shimada, K., Li, L., Deng, Y., Yai, H., Matsuki, A., Qin, Y., and Zhao, J.: Comparison of Aerosol

598   Hygroscopcity, Volatility, and Chemical Composition between a Suburban Site in the Pearl River Delta

599   Region and a Marine Site in Okinawa, Aerosol Air Qual Res, 17, 3194-3208,

600   doi:https://doi.org/10.4209/aaqr.2017.01.0020, 2017.

601   Cai, M. F., Liang, B. L., Sun, Q. B., Zhou, S. Z., Chen, X. Y., Yuan, B., Shao, M., Tan, H. B., and

602   Zhao, J.: Effects of continental emissions on cloud condensation nuclei (CCN) activity in the northern

603   South China Sea during summertime 2018, Atmos. Chem. Phys., 20, 9153-9167,

604   doi:https://doi.org/10.5194/acp-20-9153-2020, 2020.

605   Cai, M. F., Tan, H. B., Chan, C. K., Qin, Y. M., Xu, H. B., Li, F., Schurman, M. I., Liu, L., and Zhao,

606   J.: The size-resolved cloud condensation nuclei (CCN) activity and its prediction based on aerosol

607   hygroscopicity and composition in the Pearl Delta River (PRD) region during wintertime 2014, Atmos.

608   Chem. Phys., 18, 16419-16437, doi:https://doi.org/10.5194/acp-18-16419-2018, 2018.

609   Chao, Q., Xiao, C., Li, w., Wang, L., Sun, L., Chen, X., Chen, Y., Li, Y., Gao, G., Liu, Y., Zhang,

610   D., Ai, W., Chen, Y., Cui, T., Dai, T., Feng, A., Guo, Y., Huang, D., Jiang, Y., Li, D., Li, M., Liu, B., Liu,

611   Y., Lv, Z., Mei, m., Wang, Q., Wang, Y., Yin, Y., Zeng, H., Zhang, Y., Zhai, J., Zhao, L., Zhi, R., Zhong,

612   H., Zhou, X., Zhou, X., Zhu, X., and Wu, H.: China Climate Bulletin (2022), China Meteorological

613   Administration, https://www.cma.gov.cn/zfxxgk/gknr/qxbg/202303/t20230324_5396394.html, 2022.

614   Choi, Y., Rhee, T. S., Collett, J. L., Park, T., Park, S.-M., Seo, B.-K., Park, G., Park, K., and Lee, T.:

615   Aerosol concentrations and composition in the North Pacific marine boundary layer, Atmos Environ.,

616   171, 165-172, doi:https://doi.org/10.1016/j.atmosenv.2017.09.047, 2017.

617   Crosbie, E., Youn, J. S., Balch, B., Wonaschutz, A., Shingler, T., Wang, Z., Conant, W. C., Betterton,

618   E. A., and Sorooshian, A.: On the competition among aerosol number, size and composition in predicting

619   CCN variability: a multi-annual field study in an urbanized desert, Atmos Chem Phys, 15, 6943-6958,

620   doi:https://doi.org/10.5194/acp-15-6943-2015, 2015.

621   Deng, Z. Z., Zhao, C. S., Ma, N., Ran, L., Zhou, G. Q., Lu, D. R., and Zhou, X. J.: An examination

622   of parameterizations for the CCN number concentration based on in situ measurements of aerosol

623   activation properties in the North China Plain, Atmos. Chem. Phys., 13, 6227-6237,

624   doi:https://doi.org/10.5194/acp-13-6227-2013, 2013.

625   Drinovec, L., Močnik, G., Zotter, P., Prévôt, A. S. H., Ruckstuhl, C., Coz, E., Rupakheti, M., Sciare,

626   J., Müller, T., Wiedensohler, A., and Hansen, A. D. A.: The "dual-spot" Aethalometer: an

627   improved measurement of aerosol black carbon with real-time loading compensation, Atmospheric

628   Measurement Techniques, 8, 1965-1979, doi:https://doi.org/10.5194/amt-8-1965-2015, 2015.

629   Dusek, U., Frank, G. P., Hildebrandt, L., Curtius, J., Schneider, J., Walter, S., Chand, D., Drewnick,

630   F., Hings, S., Jung, D., Borrmann, S., and Andreae, M. O.: Size matters more than chemistry for cloud-

631   nucleating ability of aerosol particles, Science, 312, 1375-1378,

632   doi:https://doi.org/10.1126/science.1125261, 2006.

633   Ervens, B., Cubison, M. J., Andrews, E., Feingold, G., Ogren, J. A., Jimenez, J. L., Quinn, P. K.,

634   Bates, T. S., Wang, J., Zhang, Q., Coe, H., Flynn, M., and Allan, J. D.: CCN predictions using simplified

635   assumptions of organic aerosol composition and mixing state: a synthesis from six different locations,

636   Atmos. Chem. Phys., 10, 4795-4807, doi:https://doi.org/10.5194/acp-10-4795-2010, 2010.

637   Fitzgerald, J. W.: Dependence of the Supersaturation Spectrum of CCN on Aerosol Size Distribution

638   and Composition, J Atmos Sci, 30, 628-634, doi:https://doi.org/10.1175/1520-0469(1973)030, 1973.

639   Fletcher, Squires, I. b. P., and Bowen, F. b. E. G.: The Physics of Rainclouds, 2011.

640   Geng, X. F., Zhong, G. C., Li, J., Cheng, Z. B., Mo, Y. Z., Mao, S. D., Su, T., Jiang, H. Y., Ni, K.

641   W., and Zhang, G.: Molecular marker study of aerosols in the northern South China Sea: Impact of

642   atmospheric outflow from the Indo-China Peninsula and South China, Atmos Environ, 206, 225-236,

643   doi:https://doi.org/10.1016/j.atmosenv.2019.02.033, 2019.

644   Gras, J. L.: CN, CCN and particle size in Southern Ocean air at Cape Grim, Atmos Res, 35, 233-

645 251, doi:https://doi.org/10.1016/0169-8095(94)00021-5, 1995.

646   Gras, J. L. and Keywood, M.: Cloud condensation nuclei over the Southern Ocean: wind

647 dependence and seasonal cycles, Atmos. Chem. Phys., 17, 4419-4432, doi:https://doi.org/10.5194/acp-

648 17-4419-2017, 2017.

649   Gysel, M., Crosier, J., Topping, D. O., Whitehead, J. D., Bower, K. N., Cubison, M. J., Williams, P.

650 I., Flynn, M. J., McFiggans, G. B., and Coe, H.: Closure study between chemical composition and

651 hygroscopic growth of aerosol particles during TORCH2, Atmos. Chem. Phys., 7, 6131-6144,

652 doi:https://doi.org/10.5194/acp-7-6131-2007, 2007.

653   Heintzenberg, J.: Properties of the Log-Normal Particle Size Distribution, Aerosol Sci Tech, 21, 46-

654 48, doi:https://doi.org/10.1080/02786829408959695, 1994.

655   Huang, S., Wu, Z. J., Poulain, L., van Pinxteren, M., Merkel, M., Assmann, D., Herrmann, H., and

656 Wiedensohler, A.: Source apportionment of the organic aerosol over the Atlantic Ocean from 53 degrees

657 N to 53 degrees S: significant contributions from marine emissions and long-range transport, Atmos.

658 Chem. Phys., 18, 18043-18062,doi: 10.5194/acp-18-18043-2018, 2018

659   Huang, S., Wu, Z., Wang, Y., Poulain, L., Höpner, F., Merkel, M., Herrmann, H., and Wiedensohler,

660 A.: Aerosol Hygroscopicity and its Link to Chemical Composition in a Remote Marine Environment

661 Based on Three Transatlantic Measurements, Environ. Sci. Technol, 56, 9613-9622,

662 doi:https://doi.org/10.1021/acs.est.2c00785, 2022.

663   Hussein, T., Dal Maso, M., Petäjä, T., Koponen, I., Paatero, P., Aalto, P., Hämeri, K., and Kulmala,

664 M.: Evaluation of an automatic algorithm for fitting the particle number size distribution, Boreal Env.

665 Res, 10, 337-355, 2005

666   Ipcc: Annex I: Observational Products [Trewin, B. (ed.)], in: Climate Change 2021: The Physical

667 Science Basis. Contribution of Working Group I to the Sixth Assessment Report of the Intergovernmental

668 Panel on Climate Change, edited by: Masson-Delmotte, V., Zhai, P., Pirani, A., Connors, S. L., Péan, C.,

669 Berger, S., Caud, N., Chen, Y., Goldfarb, L., Gomis, M. I., Huang, M., Leitzell, K., Lonnoy, E., Matthews,

670 J. B. R., Maycock, T. K., Waterfield, T., Yelekçi, O., Yu, R., and Zhou, B., Cambridge University Press,

671 Cambridge, United Kingdom and New York, NY, USA, 2061–2086,

672 https://doi.org/10.1017/9781009157896.015, 2021.

673 Jimenez, J. L., Canagaratna, M. R., Donahue, N. M., Prevot, A. S., Zhang, Q., Kroll, J. H., DeCarlo,

674 P. F., Allan, J. D., Coe, H., Ng, N. L., Aiken, A. C., Docherty, K. S., Ulbrich, I. M., Grieshop, A. P.,

675 Robinson, A. L., Duplissy, J., Smith, J. D., Wilson, K. R., Lanz, V. A., Hueglin, C., Sun, Y. L., Tian, J.,

676 Laaksonen, A., Raatikainen, T., Rautiainen, J., Vaattovaara, P., Ehn, M., Kulmala, M., Tomlinson, J. M.,

677 Collins, D. R., Cubison, M. J., Dunlea, E. J., Huffman, J. A., Onasch, T. B., Alfarra, M. R., Williams, P.

678 I., Bower, K., Kondo, Y., Schneider, J., Drewnick, F., Borrmann, S., Weimer, S., Demerjian, K., Salcedo,

679 D., Cottrell, L., Griffin, R., Takami, A., Miyoshi, T., Hatakeyama, S., Shimono, A., Sun, J. Y., Zhang, Y.

680 M., Dzepina, K., Kimmel, J. R., Sueper, D., Jayne, J. T., Herndon, S. C., Trimborn, A. M., Williams, L.

681 R., Wood, E. C., Middlebrook, A. M., Kolb, C. E., Baltensperger, U., and Worsnop, D. R.: Evolution of

682 organic aerosols in the atmosphere, Science, 326, 1525-1529,

683 doi:https://doi.org/10.1126/science.1180353, 2009.

684 Kawana, K., Miyazaki, Y., Omori, Y., Tanimoto, H., Kagami, S., Suzuki, K., Yamashita, Y., Nishioka,

685 J., Deng, Y. G., Yai, H., and Mochida, M.: Number-Size Distribution and CCN Activity of Atmospheric

686 Aerosols in the Western North Pacific During Spring Pre-Bloom Period: Influences of Terrestrial and

687 Marine Sources, J Geophys Res-Atmos, 127, e2022JD036690,

688 doi:https://doi.org/10.1029/2022JD036690, 2022.

689 Köhler, H.: The nucleus in and the growth of hygroscopic droplets, Trans. Faraday Soc., 32, 1152-

690 1161, doi:https://doi.org/10.1039/TF9363201152, 1936.

691 Kouvarakis, G. and Mihalopoulos, N.: Seasonal variation of dimethylsulfide in the gas phase and

692 of methanesulfonate and non-sea-salt sulfate in the aerosols phase in the Eastern Mediterranean

693 atmosphere, Atmos Environ., 36, 929-938, doi:https://doi.org/10.1016/s1352-2310(01)00511-8, 2002.

694 Lambe, A. T., Onasch, T. B., Massoli, P., Croasdale, D. R., Wright, J. P., Ahern, A. T., Williams, L.

695 R., Worsnop, D. R., Brune, W. H., and Davidovits, P.: Laboratory studies of the chemical composition

696 and cloud condensation nuclei (CCN) activity of secondary organic aerosol (SOA) and oxidized primary

697 organic aerosol (OPOA), Atmos. Chem. Phys., 11, 8913-8928, doi:https://doi.org/10.5194/acp-11-8913-

698 2011, 2011.

Lathem, T. L. and Nenes, A.: Water Vapor Depletion in the DMT Continuous-Flow CCN Chamber: Effects on Supersaturation and Droplet Growth, Aerosol Sci Tech, 45, 604-615, doi:https://doi.org/10.1080/02786826.2010.551146, 2011.

Leena, P. P., Pandithurai, G., Anilkumar, V., Murugavel, P., Sonbawne, S. M., and Dani, K. K.: Seasonal variability in aerosol, CCN and their relationship observed at a high altitude site in Western Ghats, Meteorol Atmos Phys, 128, 143-153, doi:https://doi.org/10.1007/s00703-015-0406-0, 2016.

Liang, B., Cai, M., Sun, Q., Zhou, S., and Zhao, J.: Source apportionment of marine atmospheric aerosols in northern South China Sea during summertime 2018, Environ. Pollut, 289, 117948, doi:https://doi.org/10.1016/j.envpol.2021.117948, 2021.

Liu, P., Song, M., Zhao, T., Gunthe, S. S., Ham, S., He, Y., Qin, Y. M., Gong, Z., Amorim, J. C., Bertram, A. K., and Martin, S. T.: Resolving the mechanisms of hygroscopic growth and cloud condensation nuclei activity for organic particulate matter, Nat. Commun, 9, 4076, doi:https://doi.org/10.1038/s41467-018-06622-2, 2018.

Liu, X. and Wang, J.: How important is organic aerosol hygroscopicity to aerosol indirect forcing?, Environ. Res. Lett, 5, 044010, doi:https://doi.org/10.1088/1748-9326/5/4/044010, 2010.

Liu, Y., Sun, L., Zhou, X., Luo, Y., Huang, W., Yang, C., Wang, Y., and Huang, T.: A 1400-year terrigenous dust record on a coral island in South China Sea, Sci Rep, 4, 4994, doi:https://doi.org/10.1038/srep04994, 2014.

Meng, J. W., Yeung, M. C., Li, Y. J., Lee, B. Y. L., and Chan, C. K.: Size-resolved cloud condensation nuclei (CCN) activity and closure analysis at the HKUST Supersite in Hong Kong, Atmos. Chem. Phys., 14, 10267-10282, doi:https://doi.org/10.5194/acp-14-10267-2014, 2014.

Miller, R. M., Rauber, R. M., Di Girolamo, L., Rilloraza, M., Fu, D., McFarquhar, G. M., Nesbitt, S. W., Ziemba, L. D., Woods, S., and Thornhill, K. L.: Influence of natural and anthropogenic aerosols on cloud base droplet size distributions in clouds over the South China Sea and West Pacific, Atmos. Chem. Phys., 23, 8959-8977, doi:https://doi.org/10.5194/acp-23-8959-2023, 2023.

724   Moore, R. H., Nenes, A., and Medina, J.: Scanning Mobility CCN Analysis-A Method for Fast

725   Measurements of Size-Resolved CCN Distributions and Activation Kinetics, Aerosol Sci Tech, 44, 861-

726   871, doi:https://doi.org/10.1080/02786826.2010.498715, 2010.

727   Ou, H., Cai, M., Zhang, Y., Ni, X., Liang, B., Sun, Q., Mai, S., Sun, C., Zhou, S., Wang, H., Sun, j.,

728   and Zhao, J.: Measurement Report: Seasonal variation and anthropogenic influence on cloud

729   condensation nuclei (CCN) activity in the South China Sea: Insights from shipborne observations during

730   summer and winter of 2021 [dataset], doi:https://doi.org/10.6084/m9.figshare.25472545, 2024.

731   Ovadnevaite, J., Zuend, A., Laaksonen, A., Sanchez, K. J., Roberts, G., Ceburnis, D., Decesari, S.,

732   Rinaldi, M., Hodas, N., Facchini, M. C., Seinfeld, J. H., and O' Dowd, C.: Surface tension prevails over

733   solute effect in organic-influenced cloud droplet activation, Nature, 546, 637-641,

734   doi:https://doi.org/10.1038/nature22806, 2017.

735   Padró, L. T., Moore, R. H., Zhang, X., Rastogi, N., Weber, R. J., and Nenes, A.: Mixing state and

736   compositional effects on CCN activity and droplet growth kinetics of size-resolved CCN in an urban

737   environment, Atmos. Chem. Phys., 12, 10239-10255, doi:https://doi.org/10.5194/acp-12-10239-2012,

738   2012.

739   Park, M., Yum, S. S., Kim, N., Cha, J. W., Shin, B., and Ryoo, S.-B.: Characterization of submicron

740   aerosols and CCN over the Yellow Sea measured onboard the Gisang 1 research vessel using the positive

741   matrix   factorization   analysis   method,   Atmos   Res,   214,   430-441,

742   doi:https://doi.org/10.1016/j.atmosres.2018.08.015, 2018.

743   Patel, P. N. and Jiang, J. H.: Cloud condensation nuclei characteristics at the Southern Great Plains

744   site: role of particle size distribution and aerosol hygroscopicity, Environ Res Commun, 3,

745   doi:https://doi.org/10.1088/2515-7620/ac0e0b, 2021

746   Petters, M. D. and Kreidenweis, S. M.: A single parameter representation of hygroscopic growth

747   and   cloud   condensation   nucleus   activity,   Atmos.   Chem.   Phys.,   7,   1961-1971,

748   doi:https://doi.org/10.5194/acp-7-1961-2007, 2007.

749   Pöhlker, M. L., Pöhlker, C., Ditas, F., Klimach, T., Hrabe de Angelis, I., Araújo, A., Brito, J.,

750   Carbone, S., Cheng, Y., Chi, X., Ditz, R., Gunthe, S. S., Kesselmeier, J., Könemann, T., Lavrič, J. V.,

751 Martin, S. T., Mikhailov, E., Moran-Zuloaga, D., Rose, D., Saturno, J., Su, H., Thalman, R., Walter, D.,

752 Wang, J., Wolff, S., Barbosa, H. M. J., Artaxo, P., Andreae, M. O., and Pöschl, U.: Long-term

753 observations of cloud condensation nuclei in the Amazon rain forest – Part 1: Aerosol size distribution,

754 hygroscopicity, and new model parametrizations for CCN prediction, Atmos. Chem. Phys., 16, 15709-

755 15740, doi:https://doi.org/10.5194/acp-16-15709-2016, 2016.

756 Qin, Y., Wang, H., Wang, Y., Lu, X., Tang, H., Zhang, J., Li, L., and Fan, S.: Wildfires in Southeast

757 Asia pollute the atmosphere in the northern South China Sea, Sci Bull (Beijing), 69, 1011-1015,

758 doi:https://doi.org/10.1016/j.scib.2024.02.026, 2024.

759 Quinn, P. K., Bates, T. S., Coffman, D. J., and Covert, D. S.: Influence of particle size and chemistry

760 on the cloud nucleating properties of aerosols, Atmos. Chem. Phys., 8, 1029-1042,

761 doi:https://doi.org/10.5194/acp-8-1029-2008, 2008.

762 Quinn, P. K., Bates, T. S., Coffman, D. J., Upchurch, L., Johnson, J. E., Moore, R., Ziemba, L., Bell,

763 T. G., Saltzman, E. S., Graff, J., and Behrenfeld, M. J.: Seasonal Variations in Western North Atlantic

764 Remote Marine Aerosol Properties, J Geophys Res-Atmos, 124, 14240-14261,

765 doi:https://doi.org/10.1029/2019jd031740, 2019.

766 Rose, D., Nowak, A., Achtert, P., Wiedensohler, A., Hu, M., Shao, M., Zhang, Y., Andreae, M. O.,

767 and Poschl, U.: Cloud condensation nuclei in polluted air and biomass burning smoke near the mega-city

768 Guangzhou, China - Part 1: Size-resolved measurements and implications for the modeling of aerosol

769 particle hygroscopicity and CCN activity, Atmos. Chem. Phys., 10, 3365-3383,

770 doi:https://doi.org/10.5194/acp-10-3365-2010, 2010.

771 Ross, K. E., Piketh, S. J., Bruintjes, R. T., Burger, R. P., Swap, R. J., and Annegarn, H. J.: Spatial

772 and seasonal variations in CCN distribution and the aerosol-CCN relationship over southern Africa, J

773 Geophys Res-Atmos, 108, doi:https://doi.org/10.1029/2002jd002384, 2003.

774 Safai, P. D., Raju, M. P., Rao, P. S. P., and Pandithurai, G.: Characterization of carbonaceous aerosols

775 over the urban tropical location and a new approach to evaluate their climatic importance, Atmos Environ,

776 92, 493-500, doi:https://doi.org/10.1016/j.atmosenv.2014.04.055, 2014.

777   Sarangi, B., Ramachandran, S., Rajesh, T. A., and Dhaker, V. K.: Black carbon linked aerosol

778   hygroscopic growth: Size and mixing state are crucial, Atmos Environ., 200, 110-118,

779   doi:https://doi.org/https://doi.org/10.1016/j.atmosenv.2018.12.001, 2019.

780   Schmale, J., Henning, S., Decesari, S., Henzing, B., Keskinen, H., Sellegri, K., Ovadnevaite, J.,

781   Pohlker, M. L., Brito, J., Bougiatioti, A., Kristensson, A., Kalivitis, N., Stavroulas, I., Carbone, S.,

782   Jefferson, A., Park, M., Schlag, P., Iwamoto, Y., Aalto, P., Aijala, M., Bukowiecki, N., Ehn, M., Frank,

783   G., Frohlich, R., Frumau, A., Herrmann, E., Herrmann, H., Holzinger, R., Kos, G., Kulmala, M.,

784   Mihalopoulos, N., Nenes, A., O'Dowd, C., Petaja, T., Picard, D., Pohlker, C., Poschl, U., Poulain, L.,

785   Prevot, A. S. H., Swietlicki, E., Andreae, M. O., Artaxo, P., Wiedensohler, A., Ogren, J., Matsuki, A.,

786   Yum, S. S., Stratmann, F., Baltensperger, U., and Gysel, M.: Long-term cloud condensation nuclei

787   number concentration, particle number size distribution and chemical composition measurements at

788   regionally   representative   observatories,   Atmos.   Chem.   Phys.,   18,   2853-2881,

789   doi:https://doi.org/10.5194/acp-18-2853-2018, 2018.

790   Seinfeld, J. H. and Pandis, S. N.: Atmospheric Chemistry and Physics: From Air Pollution to

791   Climate Change, Wiley2016.

792   Sihto, S. L., Mikkila, J., Vanhanen, J., Ehn, M., Liao, L., Lehtipalo, K., Aalto, P. P., Duplissy, J.,

793   Petaja, T., Kerminen, V. M., Boy, M., and Kulmala, M.: Seasonal variation of CCN concentrations and

794   aerosol   activation   properties   in   boreal   forest,   Atmos.   Chem.   Phys.,   11,   13269-13285,

795   doi:https://doi.org/10.5194/acp-11-13269-2011, 2011.

796   Su, H., Rose, D., Cheng, Y. F., Gunthe, S. S., Massling, A., Stock, M., Wiedensohler, A., Andreae,

797   M. O., and Pöschl, U.: Hygroscopicity distribution concept for measurement data analysis and modeling

798   of aerosol particle mixing state with regard to hygroscopic growth and CCN activation, Atmos. Chem.

799   Phys., 10, 7489-7503, doi:https://doi.org/10.5194/acp-10-7489-2010, 2010.

800   Sun, C., Zhang, Y., Liang, B., Gao, M., Sun, X., Li, F., Ni, X., Sun, Q., Ou, H., Chen, D., Zhou, S.,

801   and Zhao, J.: Morphological and optical properties of carbonaceous aerosol particles from ship emissions

802   and biomass burning during a summer cruise measurement in the South China Sea, Atmos. Chem. Phys.,

803   24, 3043-3063, doi:https://doi.org/10.5194/acp-24-3043-2024, 2024.

804   Sun, Q., Liang, B., Cai, M., Zhang, Y., Ou, H., Ni, X., Sun, X., Han, B., Deng, X., Zhou, S., and

805   Zhao, J.: Cruise observation of the marine atmosphere and ship emissions in South China Sea: Aerosol

806   composition,   sources,   and   the   aging   process,   Environ.   Pollut,   316,   120539,

807   doi:https://doi.org/10.1016/j.envpol.2022.120539, 2023.

808   Wang, B., Huang, F., Wu, Z., Yang, J., Fu, X., and Kikuchi, K.: Multi-scale climate variability of

809   the   South   China   Sea   monsoon: A   review,   Dynam   Atmos   Oceans,   47,   15-37,

810   doi:https://doi.org/10.1016/j.dynatmoce.2008.09.004, 2009.Wang, Y., Chen, J., Wang, Q., Qin, Q., Ye, J.,

811   Han, Y., Li, L., Zhen, W., Zhi, Q., Zhang, Y., and Cao, J.: Increased secondary aerosol contribution and

812   possible   processing   on   polluted   winter   days   in   China,   Environ   Int,   127,   78-84,

813   doi:https://doi.org/10.1016/j.envint.2019.03.021, 2019.

814   Wang, J., Cubison, M. J., Aiken, A. C., Jimenez, J. L., and Collins, D. R.: The importance of aerosol

815   mixing state and size-resolved composition on CCN concentration and the variation of the importance

816   with   atmospheric   aging   of   aerosols,   Atmos.   Chem.   Phys.,   10,   7267-7283,

817   doi:https://doi.org/10.5194/acp-10-7267-2010, 2010.

818   Wang, Q., and Sun, Y.: Characterization of aerosol hygroscopicity, mixing state, and CCN activity

819   at a suburban site in the central North China Plain, Atmos. Chem. Phys., 18, 11739-11752,

820   doi:https://doi.org/10.5194/acp-18-11739-2018, 2018.

821   Wang, Y. Q.: MeteoInfo: GIS software for meteorological data visualization and analysis, Meteorol.

822   Appl, 21, 360-368, doi:https://doi.org/10.1002/met.1345, 2014.

823   Xiao, H.-W., Xiao, H.-Y., Luo, L., Shen, C.-Y., Long, A.-M., Chen, L., Long, Z.-H., and Li, D.-N.:

824   Atmospheric aerosol compositions over the South China Sea: temporal variability and source

825   apportionment, Atmos. Chem. Phys., 17, 3199-3214, doi:https://doi.org/10.5194/acp-17-3199-2017,

826   2017.

827   Zheng, G., Kuang, C., Uin, J., Watson, T., and Wang, J.: Large contribution of organics to

828   condensational growth and formation of cloud condensation nuclei (CCN) in the remote marine boundary

829   layer, Atmos. Chem. Phys., 20, 12515-12525, doi:https://doi.org/10.5194/acp-20-12515-2020, 2020.

830   Zhu, K. and Wang, L.: A comprehensive study on the validation and application of multi-lognormal

831   distribution   models   for   atmospheric   particles,   Atmos   Environ.,   338,   120813,

832   doi:https://doi.org/10.1016/j.atmosenv.2024.120813, 2024.

833

Location	period	N_{CN} (cm^{-3})	N_{CCN} (cm^{-3})	Hygroscopicity (κ)	Bulk AR	D_{50} (nm)	Reference
South China Sea	2021.05.05-2021.06.09	6966±9249	2640±3639 (0.20% SS) 4392±6415 (0.40% SS) 5215±6862 (0.70% SS)	0.47±0.21 (0.20% SS) 0.54±0.21 (0.40% SS)	0.37±0.16 (0.20% SS) 0.63±0.17 (0.40% SS) 0.87±0.17 (0.70% SS)	96±19 (0.20% SS) 57±9 (0.40% SS)	This study
Northern South China Sea	2021.12.19-2021.12.29	4988±3474	1086±691 (0.10% SS) 1625±1110 (0.20% SS) 2218±1503 (0.40% SS) 2797±1883 (0.70% SS)	0.50±0.21 (0.10% SS) 0.31±0.10 (0.20% SS) 0.19±0.05 (0.40% SS) 0.15±0.05 (0.70% SS)	0.23±0.09 (0.10% SS) 0.33±0.12 (0.20% SS) 0.44±0.13 (0.40% SS) 0.55±0.14 (0.70% SS)	145±18 (0.10% SS) 107±13 (0.20% SS) 79±7 (0.40 % SS) 59±6 (0.70% SS)	This study
Northern South China Sea	2018.08.06-2018.08.27	3463	1544 (0.34% SS)	0.38±0.09 (0.18% SS) 0.40±0.08 (0.34% SS) 0.38±0.08 (0.59% SS)	/	/	Cai et al., 2020
Remote South China Sea	2012.09.14-2012.09.26	503±455	450±388 (0.14% SS) 675±516 (0.38% SS) 698±555 (0.53% SS) 724±512 (0.71% SS)	0.54±0.14 (0.14% SS) 0.50±0.21 (0.38% SS)	0.47±0.16 (0.14% SS) 0.72±0.17 (0.38% SS) 0.79±0.15 (0.53% SS) 0.85±0.13 (0.71% SS)	/	Atwood et al., 2017
Western North Pacific	2015.03.04-2015.03.26	/	/	0.75±0.21 (0.11% SS) 0.51±0.16 (0.24% SS) 0.45±0.16 (0.60% SS)	0.40±0.22 (0.11% SS) 0.50±0.22 (0.24% SS) 0.70±0.23 (0.60% SS)	/	Kawana et al., 2020
Guangzhou	2014.11-2014.12	/	3103±1913 (0.10% SS) 5095±2972 (0.20% SS) 6524±3783 (0.40% SS) 7913±4234 (0.70% SS)	0.37±0.11 (0.10% SS) 0.29±0.09 (0.20% SS) 0.18±0.07 (0.40% SS) 0.15±0.06 (0.70% SS)	0.26±0.10 (0.10% SS) 0.41±0.14 (0.20% SS) 0.53±0.15 (0.40% SS) 0.64±0.13 (0.70% SS)	156 ± 19 (0.1% SS) 107 ± 17 (0.2% SS) 78 ± 15 (0.4% SS) 58 ± 11 (0.7% SS)	Cai et al., 2018

| Yellow Sea | 2017.04-2017.05 | 7622±4038 | 4821±1763 (0.63% SS) | / | / | / | Park et al., 2018 |

835   Table 1. The number concentration of particle and cloud condensation nuclei at different supersaturation (SS), the hygroscopicity and bulk activation ratio (AR), and activation

836   diameter (D_{50}) at different SS in different studies.

33

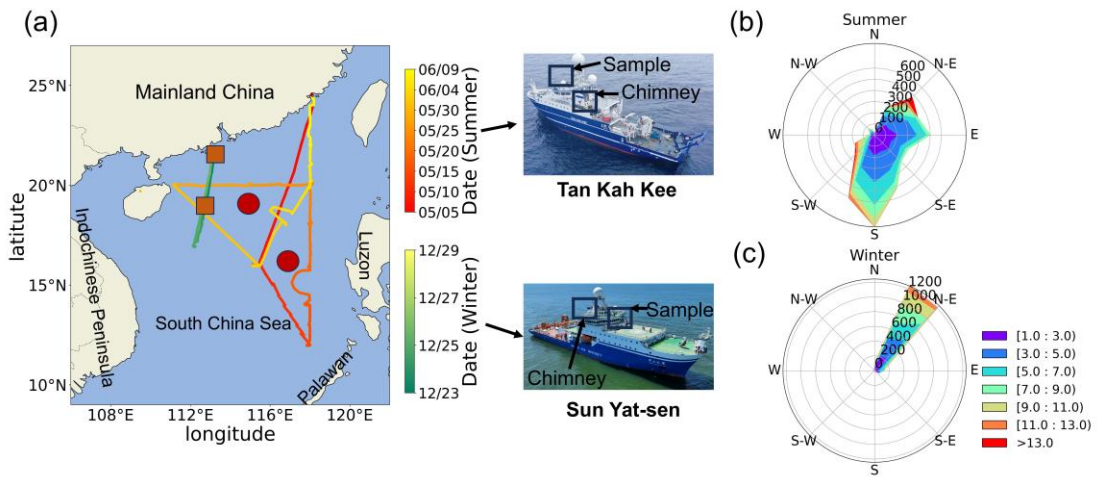|	Summer			Winter		
Cluster	Indochinese Peninsula	Luzon	Marine	Mainland China	Marine	Mixed
N_{CCN} (cm^{-3})						
0.1% SS	\	\	\	1359±669	439±223	945±400
0.2% SS	1200±787	4066±4748	1135±800	2058±1095	614±318	1460±514
0.4% SS	1650±1187	7804±8608	1812±1052	2792±1478	830±424	1801±640
0.7% SS	2239±1367	10480±9741	2515±1523	3514±1841	1024±463	2101±757
N_{CN} (cm^{-3})						
Total	2699±2147	14674±13844	3033±2366	6875±3263	1728±465	2918±1204
Nucleation	111±206	1543±3341	238±426	893±925	214±281	141±191
Aikten	1156±1261	8653±8815	1668±1526	3089±2017	732±337	806±427
Accumulation	1434±1444	3764±4157	1121±929	2923±2440	781±313	1975±831
Bulk AR						
0.1% SS	\	\	\	0.21±0.07	0.26±0.10	0.32±0.04
0.2% SS	0.49±0.13	0.31±0.17	0.40±0.13	0.30±0.09	0.36±0.14	0.51±0.05
0.4% SS	0.73±0.09	0.55±0.18	0.68±0.14	0.40±0.10	0.49±0.16	0.63±0.06
0.7% SS	0.98±0.15	0.76±0.16	0.90±0.13	0.50±0.09	0.61±0.18	0.73±0.06

838 Table 2. The number concentration of particle, cloud condensation nuclei, and bulk activation ratio in

839 different periods.

840

| Cluster	Summer			Winter		
	Luzon	Indochinese Peninsula	Marine	Mainland China	Mixed	Marine
Internal scheme						
0.1% SS	\	\	\	0.91 (0.97)	0.72 (0.95)	0.71 (0.94)
0.2% SS	0.83 (0.89)	0.89 (0.81)	0.76 (0.96)	1.13 (0.96)	1.01 (0.99)	0.94 (0.97)
0.4% SS	0.90 (0.96)	0.90 (0.98)	0.89 (0.97)	1.34 (0.97)	1.14 (0.98)	1.04 (0.98)
0.7% SS	0.91 (0.93)	0.96 (0.92)	0.88 (0.98)	1.38 (0.97)	1.16 (0.99)	1.04 (0.96)
External scheme						
0.1% SS	\	\	\	0.80 (0.97)	0.62 (0.95)	0.59 (0.94)
0.2% SS	0.74 (0.88)	0.77 (0.79)	0.80 (0.96)	1.01 (0.97)	0.90 (0.99)	0.81 (0.97)
0.4% SS	0.78 (0.93)	0.80 (0.97)	0.82 (0.96)	1.23 (0.97)	1.05 (0.98)	0.95 (0.98)
0.7% SS	0.80 (0.92)	0.89 (0.92)	0.80 (0.98)	1.24 (0.98)	1.11 (0.99)	1.00 (0.96)

842 Table 3. The slope and coefficient of determination (in parentheses) in CCN closure analysis at
843 different supersaturations in different periods.

844

845

846

847 Figure 1. The cruises of two shipborne observations, and the location of sample line and chimney of
848 Tan Kah Kee, and Sun Yat-sen scientific vessel (a); Wind rose of the wind direction and wind speed in
849 summer and winter cruises; The radius represents the frequency of wind direction occurrences, and the
850 shaded areas indicate wind speed (b) and (c). The red circles are the midpoints of the ship trajectory
851 selected for backward trajectory and cluster analysis in summer and the orange squares are the
852 midpoints of the ship trajectory selected for backward trajectory and cluster analysis in winter.
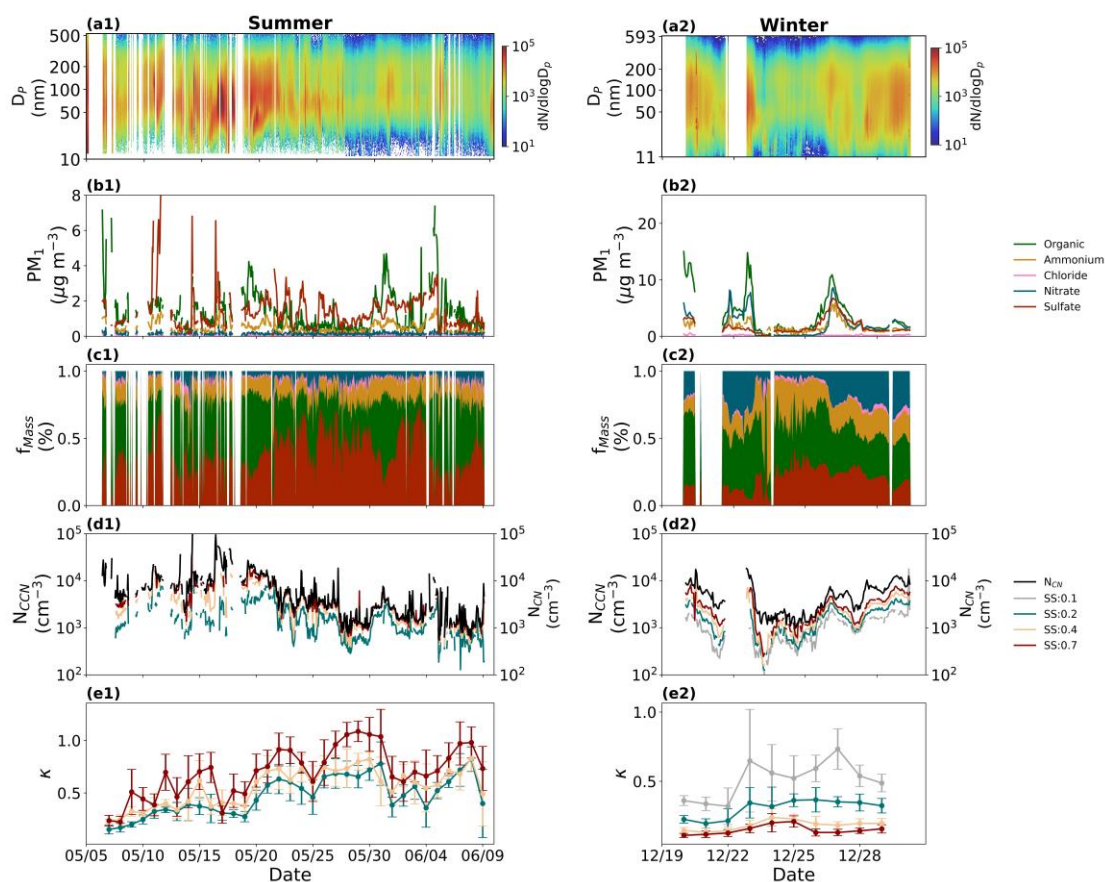
Figure 2. Timeseries of (a) particle number size distribution, (b) mass concentration of NR-PM1, and (c) its fraction, (d) mass concentration of organic carbon and elemental carbon, (e) number concentration of total particle and cloud condensation nuclei under the supersaturation of 0.1%, 0.2%, 0.4%, and 0.7%, and (f) aerosol hygroscopicity. The number 1 in figure number means timeseries in summer and number 2 means it in winter.
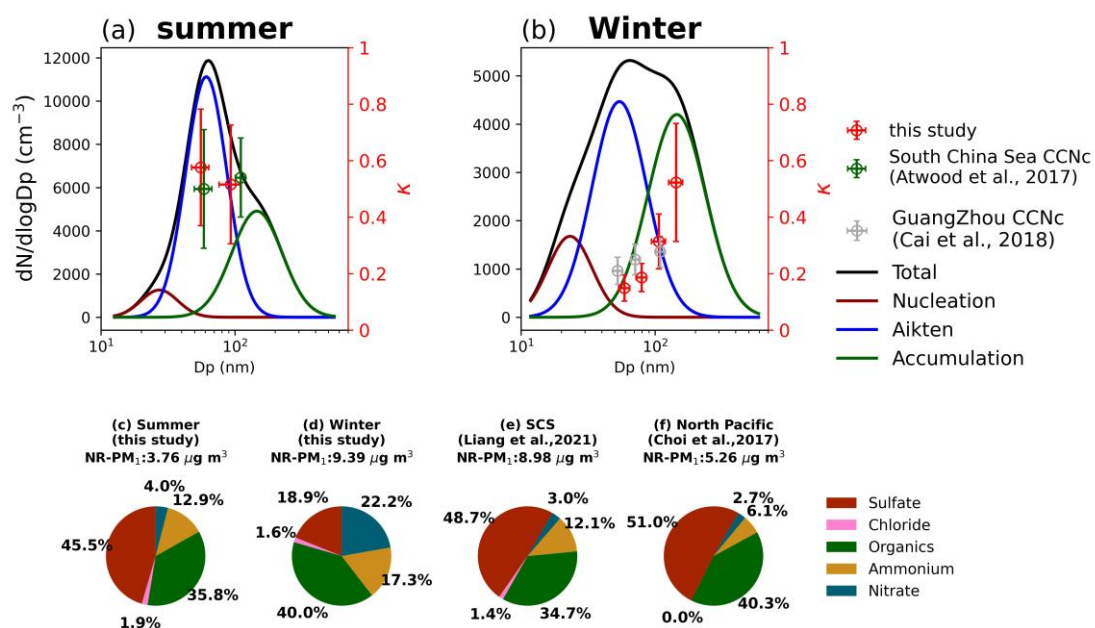
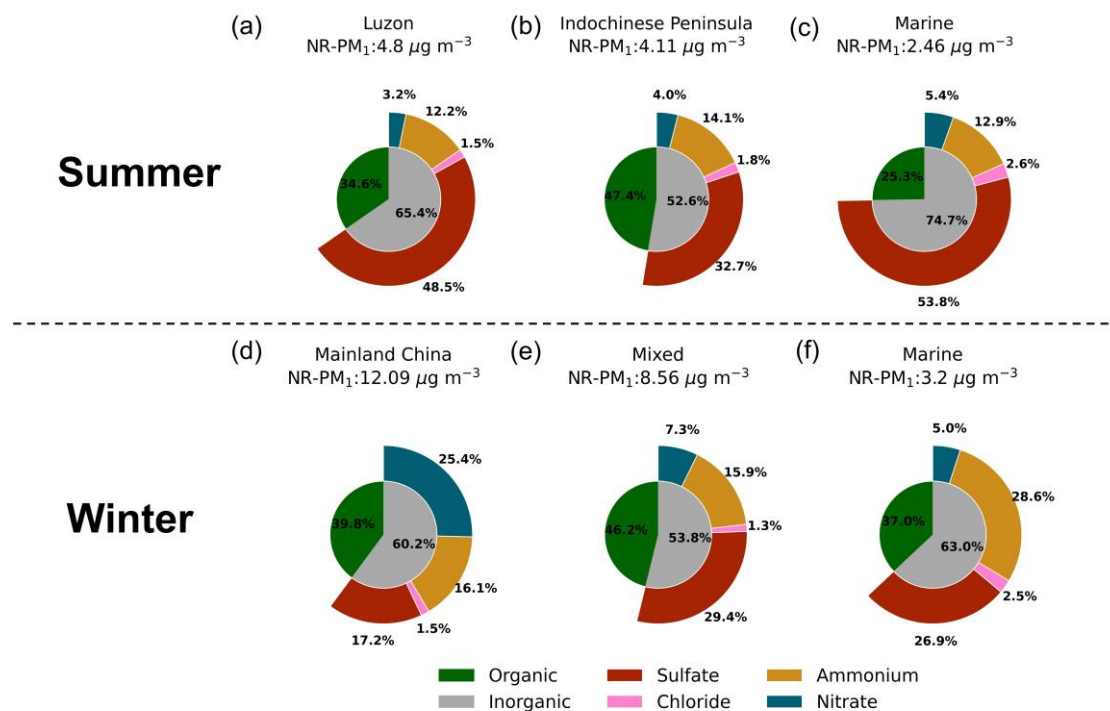Figure 3. Particle number size distribution in summer (a) and winter (b); The red markers represent the activation diameters and hygroscopicity parameters corresponding to 0.1%, 0.2%, 0.4%, and 0.7% supersaturations in this study (without 0.1% in summer). The green markers represent the hygroscopicity parameters reported in Atwood et al. (2017) for the southern South China Sea during summer. The gray markers represent the hygroscopicity parameters documented in Cai et al. (2018) for the Pearl River Delta region during winter. The fraction of NR-PM$_1$ in summer (c) and winter (d) in this study, in northern SCS reported by Liang et al. (2021) (e), and in North Pacific reported by Choi et al. (2017) (f).
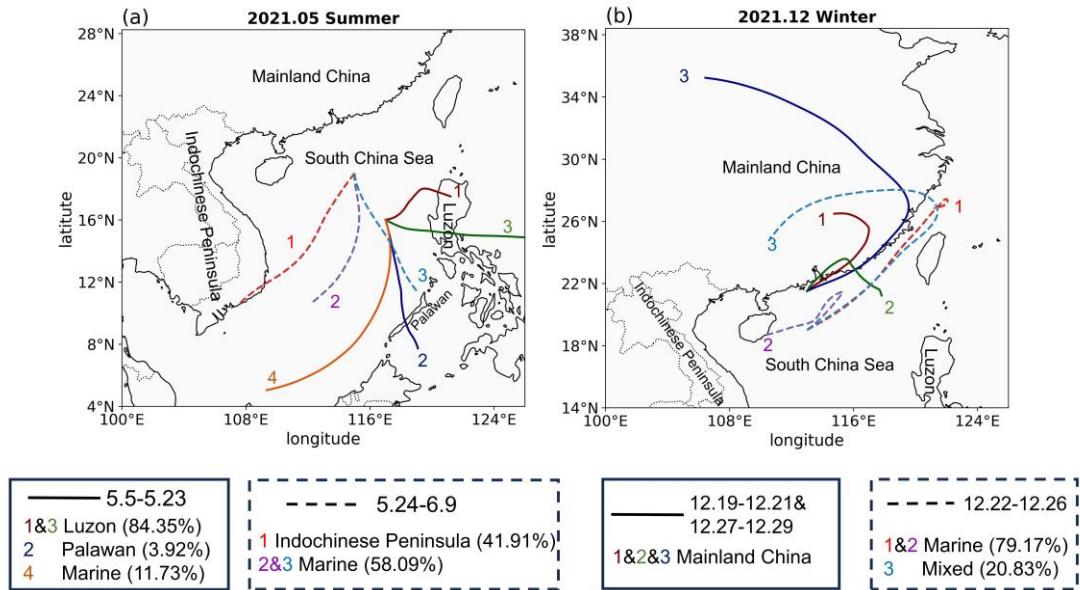
Figure 4. The cluster analysis results in summer (a) and winter (b). The solid line in summer means cluster analysis from May 5 to May 24 and the dash line in summer means cluster analysis from May 25 to June 9; The solid line in winter means cluster analysis from Dec 19 to Dec 21 and Dec 27 to Dec 29, and the dash line in winter means cluster analysis from Dec 22 to Dec 26.

Summer

(a) Luzon
NR-PM$_1$:4.8 μg m^{-3}

3.2% 12.2% 1.5%
44.6% 65.4%
48.5%

(b) Indochinese Peninsula
NR-PM$_1$:4.11 μg m^{-3}

4.0% 14.1% 1.8%
47.4% 52.6%
32.7%

(c) Marine
NR-PM$_1$:2.46 μg m^{-3}

5.4% 12.9% 2.6%
25.3% 74.7%
53.8%

Winter

(d) Mainland China
NR-PM$_1$:12.09 μg m^{-3}

25.4%
39.8% 60.2%
16.1%
17.2% 1.5%

(e) Mixed
NR-PM$_1$:8.56 μg m^{-3}

7.3% 15.9% 1.3%
46.2% 53.8%
29.4%

(f) Marine
NR-PM$_1$:3.2 μg m^{-3}

5.0% 28.6%
37.0% 63.0%
2.5%
26.9%

Organic Sulfate Ammonium
Inorganic Chloride Nitrate

876

Figure 5. The fraction of NR-PM1 in "Luzon" period (a), "Indochinese Peninsula" period (b), and "Marine-s" period (c) in summer. The fraction of NR-PM1 in "Mainland China" period (d), "Mixed" period (e), and "Marine-w" period (f) in winter.
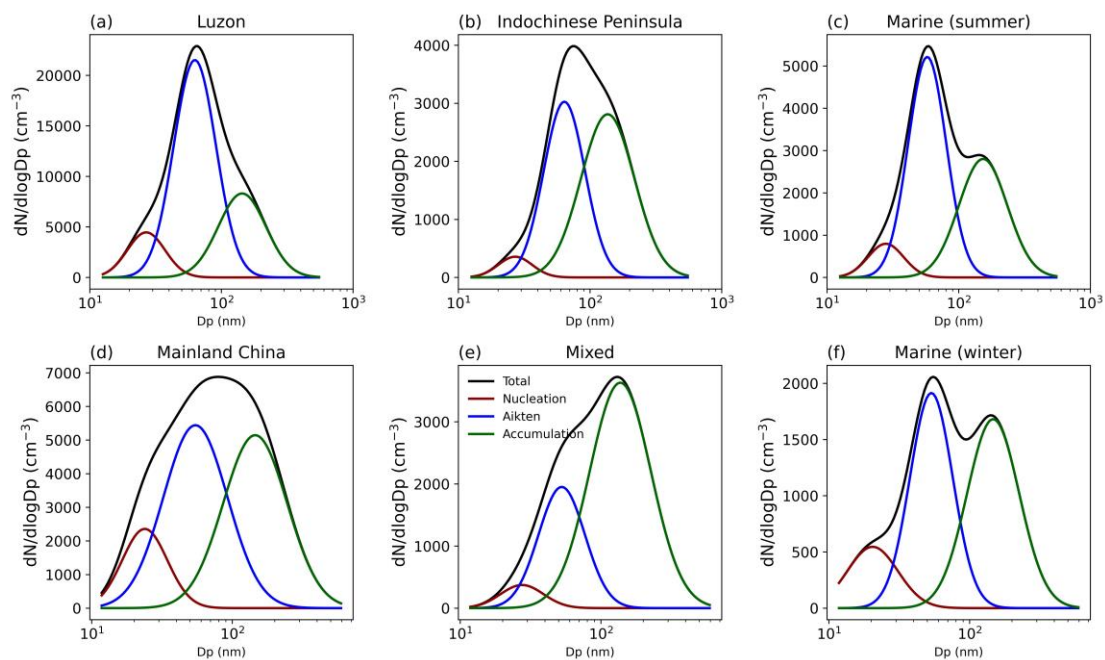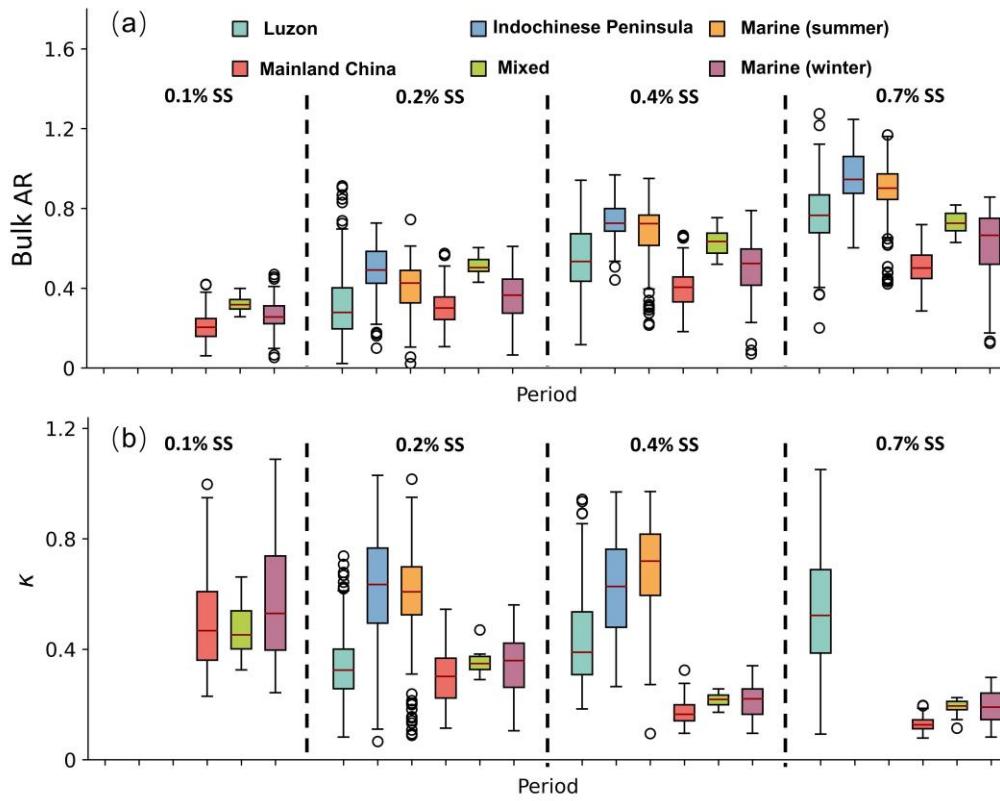
Figure 6. The particle number size distribution (PNSD) in "Luzon" period (a), "Indochinese Peninsula" period (b), and "Marine-s" period (c) in summer. The PNSD in "Mainland China" period (d), "Mixed" period (e), and "Marine-w" period (f) in winter.

885

886

887 Figure 7. The bulk activation ratio (AR) at different supersaturation (SS) in different periods (a); The

888 aerosol hygroscopicity (κ) at different supersaturation (SS) in different periods (b).
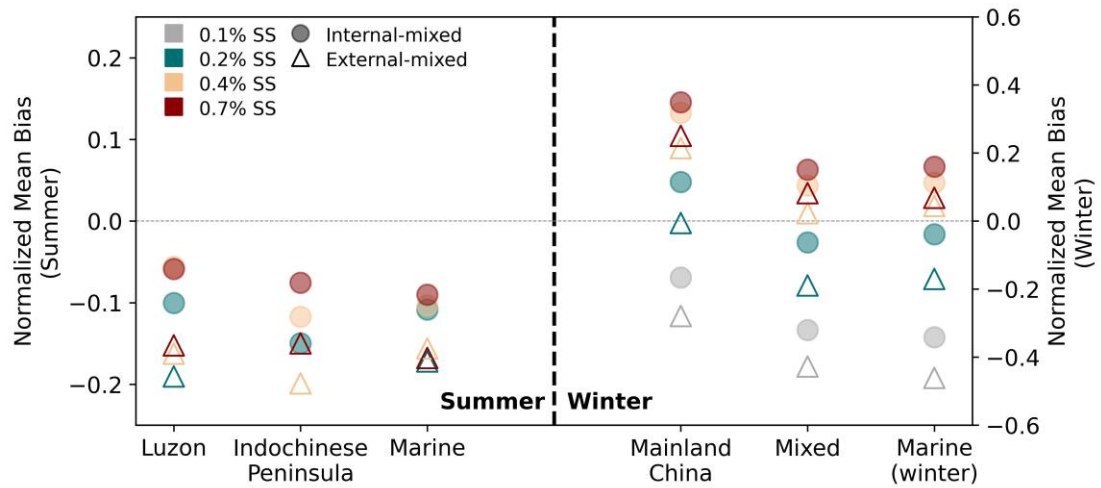
Figure 8. The normalized mean bias (NMB) calculated by "Internal-mixed" scheme and "External-mixed" scheme according to CCN closure method. The marker of circle means "Internal-mixed" scheme and the marker of triangle means "External-mixed" scheme. Different colors means different supersaturations.